

# Comparison of progenitor mass estimates for the type IIP SN 2012A

L. Tomasella,<sup>1\*</sup> E. Cappellaro,<sup>1</sup> M. Fraser,<sup>2</sup> M.L. Pumo,<sup>1</sup> A. Pastorello,<sup>1</sup>  
 G. Pignata,<sup>3</sup> S. Benetti,<sup>1</sup> F. Bufano,<sup>3</sup> M. Dennefeld,<sup>4</sup> A. Harutyunyan,<sup>5</sup> T. Iijima,<sup>1</sup>  
 A. Jerkstrand,<sup>2</sup> E. Kankare,<sup>6</sup> R. Kotak,<sup>2</sup> L. Magill,<sup>2</sup> V. Nascimbeni,<sup>7</sup>  
 P. Ochner,<sup>1</sup> A. Siviero,<sup>7</sup> S. Smartt,<sup>2</sup> J. Sollerman,<sup>8</sup> V. Stanishev,<sup>9</sup> F. Taddia,<sup>8</sup>  
 S. Taubenberger,<sup>10</sup> M. Turatto,<sup>1</sup> S. Valenti,<sup>11</sup> D.E. Wright,<sup>2</sup> L. Zampieri<sup>1</sup>

<sup>1</sup>INAF, Osservatorio Astronomico di Padova, 35122 Padova, Italy

<sup>2</sup>Astrophysics Research Centre, School of Mathematics and Physics, Queen University Belfast, Belfast BT7 1NN, UK

<sup>3</sup>Universidad Andrés Bello, Departamento Ciencias Físicas, Santiago de Chile, Chile

<sup>4</sup>Institut d'Astrophysique de Paris (IAP) and University Pierre et Marie Curie (Paris 6), Boulevard Arago F-75014 Paris, France

<sup>5</sup>Fundación Galileo Galilei, INAF Telescopio Nazionale Galileo, Rambla José Ana Fernández Pérez 7, 38712 Breña Baja, TF, Spain

<sup>6</sup>Tuorla Observatory, Department of Physics and Astronomy, University of Turku, Väisäläntie 20, FI-21500, Piikkiö, Finland

<sup>7</sup>Dipartimento di Fisica e Astronomia Galileo Galilei, Università di Padova, vicolo dell'Osservatorio 3, 35122 Padova, Italy

<sup>8</sup>The Oskar Klein Centre, Department of Astronomy, AlbaNova, SE-106 91 Stockholm, Sweden

<sup>9</sup>CENTRA Centro Multidisciplinar de Astrofísica, Instituto Superior Técnico, Av. Rovisco Pais 1, 1049-001 Lisbon, Portugal

<sup>10</sup>Max-Planck-Institut für Astrophysik, Karl-Schwarzschild-Str. 1, 85741 Garching, Germany

<sup>11</sup>Department of Physics, University of California, Santa Barbara, Broida Hall, Mail Code 9530, Santa Barbara, CA 93106-9530, USA

Released 2013 Xxxxx XX

## ABSTRACT

We present the one-year long observing campaign of SN 2012A which exploded in the nearby (9.8 Mpc) irregular galaxy NGC 3239. The photometric evolution is that of a normal type IIP supernova, but the plateau is shorter and the luminosity not as constant as in other supernovae of this type. The absolute maximum magnitude, with  $M_B = -16.23 \pm 0.16$  mag, is close to the average for SN IIP. Thanks also to the strong UV flux in the early phase, SN 2012A reached a peak luminosity of about  $2 \times 10^{42}$  erg s<sup>-1</sup>, which is brighter than those of other SNe with a similar <sup>56</sup>Ni mass. The latter was estimated from the luminosity in the exponential tail of the light curve and found to be  $M(^{56}\text{Ni}) = 0.011 \pm 0.004 M_\odot$ , which is intermediate between standard and faint SN IIP.

The spectral evolution of SN 2012A is also typical of SN IIP, from the early spectra dominated by a blue continuum and very broad ( $\sim 10^4$  km s<sup>-1</sup>) Balmer lines, to the late-photospheric spectra characterized by prominent P-Cygni features of metal lines (Fe II, Sc II, Ba II, Ti II, Ca II, Na I D). The photospheric velocity is moderately low,  $\sim 3 \times 10^3$  km s<sup>-1</sup> at 50 days, for the low optical depth metal lines. The nebular spectrum obtained 394 days after the shock breakout shows the typical features of SNe IIP and the strength of the [O I] doublet suggests a progenitor of intermediate mass, similar to SN 2004et ( $\sim 15 M_\odot$ ).

A candidate progenitor for SN 2012A has been identified in deep, pre-explosion  $K'$ -band Gemini North (NIRI) images, and found to be consistent with a star with a bolometric magnitude  $-7.08 \pm 0.36$  ( $\log L/L_\odot = 4.73 \pm 0.14$  dex). The magnitude of the recovered progenitor in archival images points toward a moderate-mass  $10.5_{-2}^{+4.5} M_\odot$  star as the precursor of SN 2012A.

The explosion parameters and progenitor mass were also estimated by means of a hydrodynamical model, fitting the bolometric light curve, the velocity and the temperature evolution. We found a best fit for a kinetic energy of 0.48 foe, an initial radius of  $1.8 \times 10^{13}$  cm and ejecta mass of  $12.5 M_\odot$ . Even including the mass for the compact remnant, this appears fully consistent with the direct measurements given above.

**Key words:** supernovae: general – supernovae: individual: SN 2012A – galaxies: individual: NGC 3239 – galaxies: abundances

## 1 INTRODUCTION

Supernovae of type IIP (SNe IIP) form a major group of core-collapse supernovae (CC SNe) characterized by a 3 – 4 months long phase of almost constant luminosity, called the plateau. These events originate from the collapse of massive stars that, at the time of explosion, retain a massive hydrogen envelope. The ejecta, that is fully ionized by the initial shock breakout, cools down with the expansion of the SN and recombines powering the long plateau phase. A number of papers have shown that SNe IIP can be fruitfully used as distance indicators. Different methods have been applied to successfully determine extragalactic distances, including the Expanding Photosphere Method (EPM; Schmidt, Kirshner, & Eastman 1992; Hamuy et al. 2001; Leonard et al. 2002; Dessart & Hillier 2005; Jones et al. 2009), the Spectral-fitting Expanding Atmosphere Model (SEAM; Baron et al. 2004) and the Standardized Candle Method (Hamuy & Pinto 2002; Nugent et al. 2006; Poznanski et al. 2009; Olivares E. et al. 2010; D’Andrea et al. 2010; Maguire et al. 2010a). The application of all of these techniques requires well monitored light curves and high-quality spectral time series. Unfortunately only a limited number of type IIP SNe fulfill the required criteria.

One well-tested approach to determine the properties of the progenitors of SNe IIP is through the modeling of the SN data with hydrodynamical codes (e.g. Grassberg, Imshennik, & Nadyozhin 1971; Falk & Arnett 1977; Litvinova & Nadezhin 1983; Blinnikov et al. 2000; Utrobin 2007; Utrobin, Chugai, & Pastorello 2007; Utrobin & Chugai 2008; Pumo & Zampieri 2011; Bersten et al. 2012). The results of type IIP SN modeling have confirmed that these SNe are produced by the explosions of massive ( $\gtrsim 10 M_{\odot}$ ) red supergiant (RSG) stars.

An alternative approach for studying CC SNe is to search for their progenitors in deep pre-explosion images (see Smartt 2009a, for a review). This has been done for a sample of SNe by Smartt et al. (2009b), who showed that the SNe IIP progenitor masses were confined to the range 8 – 17  $M_{\odot}$ , although dust effects may increase this upper limit (Walmswell & Eldridge 2012). On the other hand the theoretical expectation is that stars with masses up to 25–30  $M_{\odot}$  becomes RSGs and explode as type IIP SNe. Since no star with mass above 15–17  $M_{\odot}$  has been seen to follow this path, there is an apparent discrepancy between theory and observations that has been termed the *Red Supergiant Problem* (Smartt et al. 2009b).

However, we note that there have been claims of a discrepancy between hydrodynamical and direct progenitor mass measurements for specific SNe (Smartt 2009a) that, in view of the still large uncertainties of both approaches, leave the issue still open to discussion. Therefore any opportunities for a direct comparison between these techniques are worthy of study.

SN 2012A exploded in a very nearby host galaxy ( $D < 10$  Mpc) and is a first-rate target for studying the properties of the explosion and the progenitor star. This, and the fact that SN 2012A has good pre-explosion images available in public image archives, made this object an ideal target for an extensive follow-up campaign at multiple wavelengths. In this

national collaboration for SN research led by S. Benetti. For the composition of the Collaboration and its scientific goals, we refer the reader to our web pages (<http://graspa.oapd.inaf.it>). Observing proposals: ESO 184.D.1140; TNG AOT25\_TAC49; AOT26\_TAC46; AOT27\_TAC26. Based on observations made with the 2.56m Nordic Optical Telescope (La Palma, Spain); Copernico 1.82m Telescope (Mt. Ekar, Asiago, Italy); 2.5m Isaac Newton Telescope (La Palma, Spain); Observatoire de Haute-Provence 1.93m Telescope (France); Galileo 1.22m Telescope (Pennar, Asiago, Italy); Calar Alto Observatory 2.2m Telescope (Andalucia, Spain); 3.6m ESO NTT (La Silla, Chile); 4.2m William Herschel Telescope (La Palma, Spain); 3.6m Telescopio Nazionale Galileo (La Palma, Spain); Schmidt 67/92 Telescope (Mt. Ekar, Asiago, Italy); CTIO Prompt Telescopes (Cerro Tololo, Chile); ESO Trappist Telescope (La Silla, Chile), CN-TAC proposals CN2011B-092, CN2012A-103, CN2012B-FT-2 and CN2013A-153; ESO REM (La Silla, Chile).

paper we present the results of this monitoring campaign and discuss the implication for the SN progenitor star.

The paper is organized as follows: in Section 2 we give some information about the discovery and the follow-up observations of SN 2012A, in Section 3 we present the optical and NIR photometric evolution of SN 2012A and we compare light curves, colour curves and the computed bolometric luminosity with those of other type IIP SN. In Section 4 we analyze the spectroscopic data, in Section 5 we discuss the nature of the progenitor of this SN, both by direct detection in the pre-discovery images and by modeling of the observed data. Finally, in Sections 6 and 7 we discuss and summarize the main results of the paper.

## 2 DISCOVERY AND FOLLOW-UP OBSERVATIONS

SN 2012A was discovered by Moore et al. (2012) in an image of the irregular galaxy NGC 3239 taken on 2012 Jan 7.39 UT. The discoverers reported that the transient was not visible on 2011 Dec 29 providing a useful constraint on the explosion epoch. Spectroscopic classification obtained on Jan 10.45 UT confirmed that the transient was a type II SN close to explosion (Stanishev & Porsimo 2012). Indeed a comparison with a library of supernova spectra via the GELATO spectral classification tool (Harutyunyan et al. 2008) gives a best match with the type IIP SN 1999em (Elmhamdi et al. 2003a) soon after explosion.

The SN caught our interest when it turned out that deep, high spatial resolution predisccovery images were available allowing for the possible identification of the SN progenitor (Prieto et al. 2012, cf. Section 5.1). We immediately commenced an extensive campaign of photometric and spectroscopic monitoring that started three days after discovery and ended 407 days later.

The main information on the SN and host galaxy is reported in Table 1.

We note that the SN was also detected in *X*-rays based on *Swift* observations obtained in the first three weeks after explosion (Pooley & Immler 2012). As discussed in Section 3.4, it turned out that the *X*-ray detection corresponds to a negligible contribution to the bolometric flux.

## 3 PHOTOMETRY

Our detailed optical and infrared photometric monitoring of SN 2012A was obtained using a large number of observing facilities, listed in Table 2, where for each telescope we detail the associated instrument, the observing site, the field of view and the pixel scale.

All frames were pre-processed using standard procedures in IRAF for bias subtraction, flat fielding and astrometric calibration. For infrared exposures we also applied an illumination correction and sky background subtraction. For later epochs, multiple exposures obtained in the same night and filter were combined to improve the signal-to-noise ratio.

To measure the SN magnitude we used a dedicated pipeline developed by one of us (EC), consisting of a collection of PYTHON scripts calling standard IRAF tasks (through

**Table 1.** Main data for SN 2012A and its host galaxy, NGC 3239 from the NASA Extragalactic Database (NED). The distance modulus (Mould et al. 2000) is based on the measured redshift and using a model for the local velocity field perturbed by the influence of the Virgo cluster, the Great Attractor (GA), and the Shapley supercluster ( $H_0 = 73 \pm 5 \text{ km s}^{-1} \text{ Mpc}^{-1}$ ). The Galactic extinction is from Schlafly & Finkbeiner (2011). We measured a total extinction (Galactic plus host)  $A_B = 0.15 \text{ mag}$  (see Section 4.4).

Host galaxy	NGC 3239
Galaxy type	IB(s)m pec
Heliocentric velocity	$753 \pm 3 \text{ km s}^{-1}$
Distance modulus	$29.96 \pm 0.15 \text{ mag}$
Galactic extinction $A_B$	0.117 mag
SN type	IIP
RA(J2000.0)	$10^{\text{h}}25^{\text{m}}07.39^{\text{s}}$
Dec(J2000.0)	$+17^{\circ}09'14''.6$
Offset from nucleus	$24''65 \text{ E } 16''1 \text{ S}$
Date of discovery	2012 Jan 07.39 UT
Estimated date of explosion	$\text{MJD}=55933.0^{+1.0}_{-3.0}$
Mag at maximum	$m_V = 13.83 \pm 0.05 \text{ mag}$
$L_{\text{bol}}$ at maximum	$1.82 \times 10^{42} \text{ erg s}^{-1}$

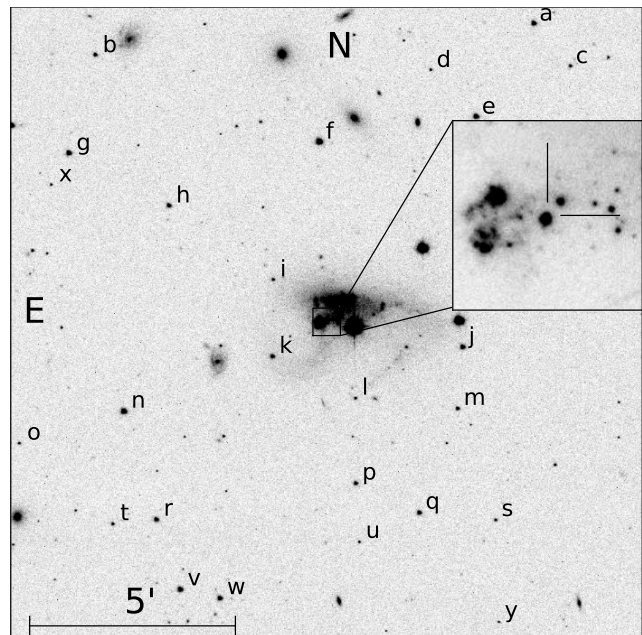


**Figure 1.** NGC 3239 and SN 2012A. The large field *V*-band image was taken with the Schmidt 67/92 telescope, Asiago, while the zoomed view of the SN region is from the Nordic Optical Telescope, La Palma. The stars of the local sequence used for the calibration of non-photometric nights are indicated.

PYRAF), and specific data analysis tools such as SEXTRACTOR for source extraction and classification, DAOPHOT for PSF fitting and HOTPANTS<sup>1</sup> for PSF matching and image subtraction.

<sup>1</sup> <http://www.astro.washington.edu/users/becker/hotpants.html>

**Table 2.** List of observing facilities employed for optical and infrared photometry.

Telescope	Instrument	Site	FoV [arcmin <sup>2</sup> ]	Scale [arcsec pix <sup>-1</sup> ]
<b>Optical facilities</b>				
Schmidt 67/92cm	SBIG	Asiago, Mount Ekar (Italy)	57 × 38	0.86
Copernico 182cm	AFOSC	Asiago, Mount Ekar (Italy)	8 × 8	0.48
Prompt 41cm	PROMPT	CTIO Observatory (Chile)	11 × 11	0.59
Calar Alto 2.2m	CAFOS	Calar Alto Observatory (Spain)	9 × 9	0.53
NOT 2.56m	ALFOSC	Roque de los Muchachos, La Palma, Canarias (Spain)	6.4 × 6.4	0.19
Trappist 60cm	TRAPPISTCAM	ESO La Silla Observatory (Chile)	27 × 27	0.65
ESO NTT 3.6m	EFOSC2	ESO La Silla Observatory (Chile)	4 × 4	0.24
TNG 3.6m	LRS	Roque de los Muchachos, La Palma, Canarias (Spain)	8 × 8	0.25
<b>Infrared facilities</b>				
REM 60cm	REMIR	ESO La Silla Observatory (Chile)	10 × 10	1.22
ESO NTT 3.6m	SOFI	ESO La Silla Observatory (Chile)	5 × 5	0.29
NOT 2.56m	NOTCAM	Roque de los Muchachos, La Palma, Canarias (Spain)	4 × 4	0.23

Following common practice for transient photometry, as a first step we calibrated a sequence of local standards in the field. To this aim we selected among our observations those obtained on photometric nights in which standard photometric fields from the list of Landolt (1992) were also observed. These observations were used to derive the zero point and colour term for each specific instrumental set-up and to calibrate the selected stars in the SN field (see Figure 1 and Table 3). The local sequence was used to calibrate non-photometric nights. For the infrared photometry we used as reference for the calibration 2MASS stars in the SN field.

The region around the SN location is crowded with many sources which require special care in the measurement of the transient instrumental magnitude, in particular when the SN becomes faint and/or the seeing is poor. As a rule, the SN magnitude was measured via PSF fitting. In our implementation of the PSF fitting procedure first the sky background at the SN location is estimated by a low order polynomial fit and subtracted from the image before performing a simultaneous fit of the SN and the nearby companion stars (that is all stellar sources in a radius of  $\sim 5 \times \text{FWHM}$  from the SN) using the PSF model derived from isolated field stars. The fitted sources are removed from the original images, an improved estimate of the local background is derived and the PSF fitting procedure iterated. The residuals are visually inspected to validate the fit.

An alternative approach for the measurement of transient magnitudes is template subtraction. The application of this technique requires exposures of the field obtained before the SN explosion or after the SN has faded. The template images need to be in the same filter and have good S/N and seeing. While in principle they should be obtained with the same telescope as the specific SN observation (to guarantee the same bandpass), in practice we are bound to what is actually available in the accessible image archives. In the case of SN 2012A we could retrieve deep pre-discovery exposures in *B*, *V*, *R* bands obtained with the Vatican Advanced Telescope Technology (VATT) and *u* and *i* band exposures from SDSS. For the *J*, *H*, *K* infrared bands we rely on moderate quality 2MASS exposures.

For template subtraction, first the template image is geometrically registered to the same pixel grid as the SN

frame, and thereafter the PSF of the two images is matched by means of a convolution kernel determined by comparing a number of reference sources in the field. After matching the photometric scale, the template image is subtracted from the SN image and a difference image is obtained where only the transient is present. Again, the instrumental magnitude of the transient in the difference image is measured through a PSF fit, where the model PSF is derived from the image with the worst seeing. It is found that the latter procedure is more robust with respect to plain aperture photometry in particular concerning the background level determination.

When we compare the PSF fitting vs. template subtraction measured magnitudes we find that they are in excellent agreement when the transient is bright. As a rule we kept the PSF fitting magnitudes when the discrepancy is  $< 0.05$  mag and instead adopted the template subtraction magnitudes when the discrepancy is larger. For the optical bands this occurs for  $\text{mag} > 18$  whereas for infrared the same threshold is  $\text{mag} > 14$ .

Error estimates were obtained through artificial star experiments in which a fake star, of magnitude similar to that of the SN, is placed in the PSF fit residual image in a position close to, but not coincident with that of the real source. The simulated image is processed through the PSF fitting procedure and the dispersion of measurements out of a number of experiments, with the fake star in slightly different positions, is taken as an estimate of the instrumental magnitude error, that mainly accounts for the background fitting uncertainty. This is combined (in quadrature) with the PSF fit error returned by DAOPHOT, and the propagated errors from the photometric calibration.

The final calibrated SN magnitudes are listed in Table 4 and 6 for the optical bands and in Table 5 for the infrared.

Our light curves were complemented with *UV*-optical photometry of SN 2012A obtained using UVOT on board of the *Swift* satellite and recently published by Pritchard et al. (2013). This includes measurements in three *UV* filters with central wavelengths in the range 1838 – 2600 Å, most useful for the derivation of the bolometric luminosity (cf. Section 3.4), as well as additional *UBV* optical photometry.

**Table 3.** Magnitudes for the local sequence stars, as indicated in Figure 1.

id	R.A.	Dec.	<i>U</i>	<i>B</i>	<i>V</i>	<i>R</i>	<i>I</i>
a	10:24:47.574	17:16:00.82	16.371 (0.027)	16.08 (0.003)	15.311 (0.003)	14.878 (0.003)	14.480 (0.004)
b	10:25:29.287	17:15:20.22	16.591 (0.017)	16.64 (0.009)	16.261 (0.006)	16.007 (0.010)	15.788 (0.011)
c	10:24:44.117	17:15:02.38	18.344 (0.036)	17.89 (0.013)	17.003 (0.014)	16.530 (0.021)	16.127 (0.011)
d	10:24:57.404	17:14:58.00	20.420 (0.117)	19.07 (0.046)	17.563 (0.017)	16.601 (0.011)	15.152 (0.016)
e	10:24:53.106	17:13:53.92	16.224 (0.027)	15.80 (0.005)	15.007 (0.005)	14.562 (0.007)	14.186 (0.009)
f	10:25:08.015	17:13:20.67	14.954 (0.026)	14.74 (0.003)	14.043 (0.004)	13.649 (0.004)	13.281 (0.005)
g	10:25:31.827	17:13:06.34	15.836 (0.015)	15.82 (0.004)	15.129 (0.003)	14.693 (0.004)	14.280 (0.006)
h	10:25:22.336	17:11:54.18	18.156 (0.027)	17.01 (0.005)	15.539 (0.011)	14.601 (0.007)	13.496 (0.010)
i	10:25:12.441	17:10:12.55	17.353 (0.029)	17.49 (0.021)	17.015 (0.010)	16.731 (0.013)	16.429 (0.016)
j	10:24:54.466	17:08:39.59	16.189 (0.027)	16.04 (0.004)	15.346 (0.006)	14.955 (0.016)	14.594 (0.011)
k	10:25:12.540	17:08:27.78	18.491 (0.038)	17.15 (0.008)	15.821 (0.005)	14.913 (0.011)	14.060 (0.007)
l	10:25:04.672	17:07:30.29	17.990 (0.033)	18.05 (0.015)	17.377 (0.013)	16.985 (0.009)	16.550 (0.034)
m	10:24:54.973	17:07:15.56	16.708 (0.028)	16.83 (0.008)	16.262 (0.002)	15.932 (0.008)	15.594 (0.011)
n	10:25:26.693	17:07:13.71	16.100 (0.016)	15.47 (0.004)	14.454 (0.005)	13.906 (0.003)	13.361 (0.002)
o	10:25:36.645	17:06:30.60	20.000 (0.038)	18.99 (0.033)	17.481 (0.017)	16.476 (0.023)	15.313 (0.022)
p	10:25:04.685	17:05:34.11	18.309 (0.036)	17.15 (0.005)	15.995 (0.009)	15.198 (0.019)	14.533 (0.007)
q	10:24:58.654	17:04:53.79	16.692 (0.028)	16.39 (0.007)	15.613 (0.007)	15.156 (0.012)	14.732 (0.005)
r	10:25:23.644	17:04:45.78	16.238 (0.027)	16.18 (0.006)	15.530 (0.009)	15.176 (0.006)	14.804 (0.009)
s	10:24:51.407	17:04:43.36	17.649 (0.030)	17.80 (0.015)	17.206 (0.015)	16.819 (0.018)	16.489 (0.019)
t	10:25:27.785	17:04:39.95	17.282 (0.029)	17.52 (0.015)	16.980 (0.006)	16.679 (0.013)	16.357 (0.019)
u	10:25:04.368	17:04:14.31	20.092 (0.093)	18.97 (0.032)	17.614 (0.018)	16.681 (0.024)	15.880 (0.013)
v	10:25:21.392	17:03:10.35	17.556 (0.021)	16.34 (0.004)	14.953 (0.009)	14.011 (0.008)	13.097 (0.005)
w	10:25:17.623	17:02:58.08	16.175 (0.017)	16.00 (0.008)	15.293 (0.007)	14.887 (0.004)	14.514 (0.009)
x	10:25:33.513	17:12:23.65	18.403 (0.029)	18.39 (0.017)	17.802 (0.021)	17.436 (0.021)	
y	10:24:51.160	17:02:24.45	20.088 (0.031)	19.16 (0.019)	18.192 (0.014)	17.535 (0.033)	

### 3.1 Photometric evolution

The multicolour light curves of SN 2012A are shown in Figure 2. We included the pre-discovery limit and the discovery and confirmation magnitudes from Moore et al. (2012) that, although unfiltered, are crucial to constrain the epoch of explosion. Indeed, when compared with our *R*-band photometry, these observations appear to describe a very steep rise to maximum and indicate MJD=55933.0<sup>+1.0</sup><sub>-3.0</sub> as the best estimate for the epoch of explosion.

In typical SNe IIP, after the fast rise, the light curve settles on a plateau phase during which the luminosity remains roughly constant, sustained by the recombination of the hydrogen envelope which was fully ionized after shock breakout. Actually, in the case of SN 2012A the luminosity in the plateau phase was never really constant: between 20 and 80 days, the magnitude decline rate is indeed small in the *K*-band [0.3 mag (100d)<sup>-1</sup>], but already significant in the *R*-band [1.0 mag (100d)<sup>-1</sup>] and is largest in the *U*-band [4.0 mag (100d)<sup>-1</sup>]. For comparison, in the same period SN 1999em (cf. Elmhamdi et al. 2003a) brightened in the *K*-band at a rate of 1.0 mag (100d)<sup>-1</sup>, declined by only 0.1 mag (100d)<sup>-1</sup> in the *R*-band and had a similar decline in the *U*-band of 5.0 mag (100d)<sup>-1</sup>.

We note that the behavior in the different bands of SN 2012A does not appear to be driven by a decrease of the photospheric temperature in the envelope that, as expected in the recombination phase, remains more or less constant (cf. Figure 11). Most likely the evolution in the plateau phase is related to changes in line opacities in the outer envelope regions.

At the end of hydrogen recombination the light curves of type IIP SNe show a sudden drop in luminosity. In the case of SN 2012A this occurs about 90 days after explosion, 15 – 20 days earlier than for SN 1999em. The period of rapid luminosity decline terminates at about 110 days after a drop in the *R*-band of  $\sim 2$  mag. After this, the light curves settle onto a much shallower linear decline powered by the radioactive decay of <sup>56</sup>Co into <sup>56</sup>Fe. Indeed, the decline rate in *V* and *R* bands measured in the phase range 150 – 400 d is 0.9 mag (100d)<sup>-1</sup>, very close to the expected energy input from <sup>56</sup>Co decay, 0.98 mag (100d)<sup>-1</sup>.

The *U* – *B*, *B* – *V*, *V* – *R*, *R* – *I* and *V* – *K* colour curves of SN 2012A are shown in Figure 3 and compared to those of SNe 1999em (Elmhamdi et al. 2003a), 2009bw (Inserra et al. 2012) and 2005cs (Pastorello et al. 2006, 2009). The choice of these SNe as references is justified by the fact that, as will be shown in the following, they appear to bracket SN 2012A in a number of properties, including luminosity, expansion velocity, temperature and <sup>56</sup>Ni-mass.

The colours of SN 2012A have been corrected for the sum of the adopted Galactic and host galaxy extinction, that is  $A_B = 0.15$  mag (cf. Section 4.4), whereas for the comparison SNe we adopted the extinction corrections given in the quoted papers. In all colours the evolution of the four SNe is remarkably similar up to 100 days from explosion. The rapid colour evolution seen in the first month (especially in the *B* – *V* colour) is a result of the expansion and cooling of the SN photosphere. After 100 – 120 days, the colours of SN 2012A show very little evolution, similar to the behaviour

**Table 4.** Optical photometry in Johnson-Cousins filters, with associated errors in parentheses.

Date	MJD	<i>U</i>	<i>B</i>	<i>V</i>	<i>R</i>	<i>I</i>	Instrument
20120110	55936.25	13.16 (0.07)	14.12 (0.02)	14.22 (0.02)	13.89 (0.04)	14.23 (0.06)	ALFOSC
20120110	55937.00		13.92 (0.02)	13.94 (0.01)	13.87 (0.02)	13.75 (0.02)	SBIG
20120111	55937.25		14.09 (0.03)	14.03 (0.04)	13.84 (0.03)	13.80 (0.02)	PROMPT
20120112	55938.03		13.94 (0.02)	13.91 (0.02)	13.79 (0.03)	13.71 (0.03)	SBIG
20120112	55938.22		14.14 (0.07)	13.99 (0.02)	13.90 (0.04)	13.78 (0.04)	PROMPT
20120112	55938.97		13.93 (0.04)	13.89 (0.03)	13.79 (0.03)	13.71 (0.02)	SBIG
20120113	55939.25		14.06 (0.03)	14.07 (0.05)	13.74 (0.04)	13.72 (0.04)	PROMPT
20120114	55940.03		13.86 (0.02)	13.85 (0.02)	13.66 (0.02)	13.65 (0.02)	SBIG
20120114	55940.26		13.94 (0.03)	14.01 (0.01)	13.82 (0.02)	13.73 (0.02)	PROMPT
20120114	55940.92		13.92 (0.02)	13.84 (0.02)	13.68 (0.03)	13.69 (0.02)	SBIG
20120115	55941.97		13.96 (0.03)	13.83 (0.02)	13.71 (0.03)	13.68 (0.02)	SBIG
20120118	55944.05		13.98 (0.04)	13.85 (0.04)	13.67 (0.03)	13.64 (0.03)	SBIG
20120121	55947.22		14.20 (0.02)	13.96 (0.01)	13.71 (0.05)	13.61 (0.02)	PROMPT
20120121	55947.93	13.85 (0.05)	14.26 (0.02)	13.97 (0.01)	13.75 (0.03)	13.70 (0.07)	AFOSC
20120123	55949.96	14.26 (0.03)	14.39 (0.02)	14.01 (0.05)	13.69 (0.03)	13.47 (0.04)	AFOSC
20120124	55950.93	14.26 (0.02)	14.33 (0.01)	13.91 (0.04)	13.60 (0.02)	13.52 (0.05)	AFOSC
20120125	55951.21		14.48 (0.26)				PROMPT
20120125	55951.93		14.37 (0.03)	13.87 (0.02)	13.63 (0.04)	13.57 (0.03)	SBIG
20120126	55952.23			14.05 (0.08)	13.78 (0.14)	13.61 (0.02)	PROMPT
20120127	55953.05	14.56 (0.04)	14.61 (0.05)	14.06 (0.03)	13.56 (0.03)	13.52 (0.04)	AFOSC
20120127	55953.88	14.63 (0.07)	14.65 (0.09)	14.11 (0.03)	13.65 (0.05)	13.55 (0.12)	AFOSC
20120129	55955.94	15.00 (0.03)	14.75 (0.04)	14.11 (0.02)	13.71 (0.02)	13.63 (0.04)	AFOSC
20120130	55956.93	15.38 (0.03)	14.81 (0.02)	14.13 (0.03)	13.79 (0.04)	13.68 (0.06)	AFOSC
20120203	55960.93			14.09 (0.04)	13.71 (0.04)	13.67 (0.04)	SBIG
20120208	55965.15			14.26 (0.10)	13.86 (0.06)		SBIG
20120208	55965.93		15.02 (0.04)	14.15 (0.03)	13.76 (0.07)	13.61 (0.05)	SBIG
20120209	55966.19		15.11 (0.04)	14.27 (0.05)	13.82 (0.05)	13.60 (0.04)	PROMPT
20120211	55968.08	15.63 (0.03)	15.20 (0.05)	14.34 (0.01)	13.86 (0.02)	13.62 (0.02)	CAFOS
20120214	55971.18		15.19 (0.03)	14.30 (0.03)	13.93 (0.04)	13.67 (0.03)	PROMPT
20120217	55974.17		15.34 (0.04)	14.38 (0.02)	13.89 (0.03)	13.60 (0.03)	PROMPT
20120217	55974.97	16.44 (0.04)	15.35 (0.02)	14.29 (0.02)	13.87 (0.05)		AFOSC
20120218	55975.97	16.28 (0.06)	15.50 (0.02)	14.43 (0.03)	13.82 (0.04)	13.66 (0.06)	AFOSC
20120221	55978.31			14.38 (0.02)	13.93 (0.04)	13.66 (0.03)	PROMPT
20120223	55980.04	16.45 (0.07)	15.53 (0.03)	14.42 (0.03)	14.00 (0.04)	13.68 (0.05)	AFOSC
20120224	55981.20		15.46 (0.03)	14.41 (0.04)	13.96 (0.03)	13.68 (0.03)	PROMPT
20120226	55983.01	16.66 (0.04)	15.50 (0.02)	14.42 (0.02)	13.81 (0.02)	13.80 (0.04)	AFOSC
20120227	55984.14		15.53 (0.05)	14.41 (0.02)	13.99 (0.03)	13.68 (0.04)	PROMPT
20120228	55985.96	16.93 (0.06)	15.62 (0.03)	14.50 (0.04)	13.97 (0.02)	13.75 (0.05)	AFOSC
20120229	55986.14		15.47 (0.14)				PROMPT
20120301	55987.14			14.48 (0.02)	14.03 (0.04)	13.74 (0.03)	PROMPT
20120304	55990.12		15.65 (0.03)	14.49 (0.03)	14.02 (0.03)	13.66 (0.02)	PROMPT
20120306	55992.13		15.57 (0.17)				PROMPT
20120306	55992.89			14.45 (0.03)	13.93 (0.03)	13.76 (0.04)	SBIG
20120312	55998.07		15.91 (0.02)	14.72 (0.03)	14.09 (0.02)	13.84 (0.04)	CAFOS
20120312	55998.11		15.73 (0.05)	14.57 (0.01)	14.11 (0.02)	13.78 (0.02)	PROMPT
20120313	55999.16	17.19 (0.06)	15.72 (0.02)	14.69 (0.04)	14.12 (0.01)	14.04 (0.05)	EFOSC
20120313	55999.80		15.70 (0.03)	14.60 (0.02)	14.10 (0.03)	13.87 (0.02)	SBIG
20120314	56000.10		15.78 (0.03)	14.59 (0.03)	14.10 (0.04)	13.83 (0.02)	PROMPT
20120314	56000.85		15.65 (0.02)	14.51 (0.02)	14.07 (0.02)	13.78 (0.02)	SBIG
20120315	56001.79		15.87 (0.02)	14.58 (0.01)	14.20 (0.03)	13.91 (0.02)	SBIG
20120316	56002.05		15.64 (0.21)				PROMPT
20120316	56002.82		15.65 (0.02)	14.52 (0.02)	14.15 (0.02)	13.79 (0.03)	SBIG
20120317	56003.04			14.71 (0.04)	14.17 (0.03)	13.95 (0.03)	PROMPT
20120317	56003.96	17.23 (0.08)	15.81 (0.03)	14.55 (0.02)	14.07 (0.04)		AFOSC
20120319	56005.12		15.83 (0.04)	14.67 (0.03)	14.19 (0.03)	13.92 (0.03)	PROMPT
20120320	56006.88		15.73 (0.05)	14.52 (0.02)	14.16 (0.04)	13.76 (0.04)	SBIG

**Table 4** – *continued* Optical photometry in Johnson-Cousins filters, with associated errors in parentheses.

Date	MJD	<i>U</i>	<i>B</i>	<i>V</i>	<i>R</i>	<i>I</i>	Instrument
20120322	56008.11		15.92 (0.03)	14.70 (0.05)	14.19 (0.02)	13.96 (0.02)	PROMPT
20120322	56008.83		15.87 (0.03)	14.66 (0.02)	14.24 (0.03)	14.04 (0.03)	SBIG
20120324	56010.07		15.93 (0.04)	14.71 (0.03)	14.25 (0.03)	13.94 (0.01)	PROMPT
20120326	56012.08		15.83 (0.14)				PROMPT
20120326	56012.84		15.89 (0.05)	14.69 (0.01)	14.28 (0.02)	13.99 (0.03)	SBIG
20120327	56013.01			14.90 (0.03)	14.35 (0.03)	14.07 (0.02)	PROMPT
20120327	56013.86		15.93 (0.03)	14.71 (0.02)	14.43 (0.07)		SBIG
20120328	56014.82		15.95 (0.05)	14.77 (0.04)	14.26 (0.05)	14.08 (0.04)	SBIG
20120329	56015.81		15.90 (0.03)	14.82 (0.02)	14.37 (0.02)	14.10 (0.03)	SBIG
20120330	56016.05		16.02 (0.03)	14.87 (0.03)	14.36 (0.03)	14.06 (0.02)	PROMPT
20120331	56017.94	17.83 (0.17)					AFOSC
20120331	56017.94		16.16 (0.04)	15.03 (0.03)	14.53 (0.01)	14.16 (0.05)	AFOSC
20120403	56020.04		16.23 (0.05)	14.96 (0.02)	14.48 (0.03)	14.14 (0.03)	PROMPT
20120409	56026.11		16.37 (0.07)	15.17 (0.03)	14.66 (0.03)	14.35 (0.01)	PROMPT
20120412	56029.08				14.80 (0.23)	14.49 (0.09)	PROMPT
20120412	56030.00		16.53 (0.02)	15.31 (0.01)	14.81 (0.03)	14.57 (0.02)	ALFOSC
20120414	56032.00		16.69 (0.02)	15.39 (0.02)	14.99 (0.02)	14.56 (0.05)	ALFOSC
20120417	56034.11			15.64 (0.03)	14.97 (0.03)	14.72 (0.02)	PROMPT
20120419	56036.00		17.13 (0.05)	15.80 (0.05)	15.13 (0.03)	14.90 (0.02)	PROMPT
20120421	56039.00		17.62 (0.10)	16.26 (0.05)	15.52 (0.04)	15.18 (0.03)	PROMPT
20120422	56039.90			16.34 (0.03)	15.49 (0.04)	15.41 (0.11)	SBIG
20120423	56040.04	> 19.40	17.87 (0.04)	16.40 (0.03)	15.67 (0.04)	15.26 (0.03)	CAFOS
20120424	56041.96	> 18.90	18.32 (0.14)	16.79 (0.05)	15.95 (0.04)		AFOSC
20120425	56042.86		18.28 (0.05)	16.77 (0.03)	16.09 (0.03)	15.70 (0.03)	SBIG
20120426	56043.86		18.64 (0.07)	17.13 (0.04)	16.22 (0.05)	15.89 (0.04)	SBIG
20120427	56044.82		18.58 (0.09)	17.23 (0.03)	16.34 (0.05)	15.90 (0.05)	SBIG
20120501	56048.85		18.90 (0.07)	17.63 (0.04)	16.61 (0.04)	16.19 (0.04)	CAFOS
20120515	56062.86		19.16 (0.15)	17.72 (0.02)	16.76 (0.03)	16.32 (0.06)	CAFOS
20120529	56077.00		19.40 (0.11)	18.02 (0.10)	17.01 (0.10)		TRAPPISTCAM
20120619	56097.99		19.48 (0.10)	18.03 (0.10)	17.15 (0.11)		TRAPPISTCAM
20121020	56220.18		20.12 (0.15)	18.99 (0.13)			AFOSC
20121021	56221.25		20.31 (0.15)	19.11 (0.14)	18.03 (0.03)	17.83 (0.03)	LRS
20121109	56240.17		20.54 (0.27)	19.37 (0.14)	18.19 (0.09)	17.95 (0.23)	AFOSC
20121122	56253.34			19.52 (0.11)	18.41 (0.12)		TRAPPISTCAM
20121207	56268.13		20.60 (0.23)	19.45 (0.15)	18.65 (0.10)	18.25 (0.14)	AFOSC
20121210	56271.15			19.55 (0.14)	18.63 (0.11)	18.45 (0.12)	AFOSC
20121212	56273.28				18.67 (0.11)		TRAPPISTCAM
20130203	56326.25		20.86 (0.15)	19.96 (0.14)	19.09 (0.14)	19.07 (0.11)	LRS
20130221	56344.24			20.07 (0.09)	19.39 (0.10)		TRAPPISTCAM

of SNe 1999em and 2009bw, whereas SN 2005cs shows a sudden jump to somewhat redder colours that is a characteristic feature of many faint type II SNe (Pastorello et al. 2009).

### 3.2 The *ugriz* photometry

An increasing number of observing facilities are equipped with *ugriz* filters which mimic the photometric system of the Sloan Digital Sky Survey<sup>2</sup>. Therefore one is often faced with the problem of comparing SDSS-like photometry for a SN with the template light curves available in the conventional *UBVRI* Johnson-Cousins system. Transformation equations have been provided by a number of authors, derived from comparisons of the magnitudes of standard stars in the two photometric systems (Chonis & Gaskell 2008, and reference

therein). However SN spectra are very different from those of typical stars, with strong absorptions and emissions, and so the validity of these transformation equations is not guaranteed.

For SN 2012A, in many respects a typical type IIP SN, we have the opportunity of direct testing the validity of these transformation equations, thanks to simultaneous observations in both systems obtained with the PROMPT telescopes at CTIO.

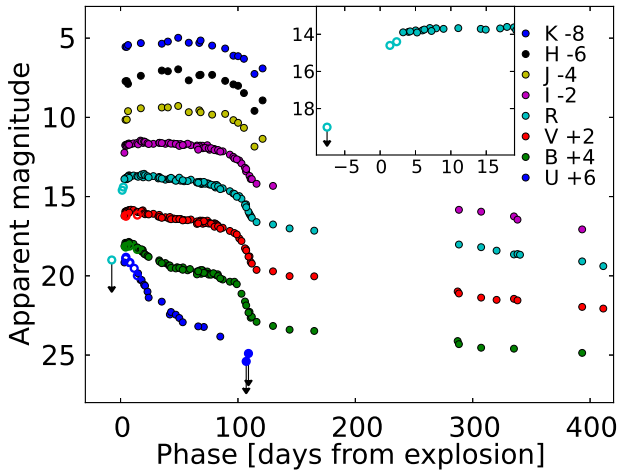
The *griz* photometry of SN 2012A, reduced with the same recipes as for the Johnson-Cousins photometry, is reported in Table 6. The photometric calibration was obtained by comparison with the SDSS magnitudes for the stars in the field of the SN and are therefore close to the AB system ( $SDSS = AB - 0.02$  mag), whereas the Johnson-Cousins photometry reported in Table 4 are in the VEGA system.

In Figure 4 we show the difference in SN magnitude in the SDSS and Johnson-Cousins systems for selected fil-

<sup>2</sup> <http://www.sdss.org>

**Table 5.** Infrared photometry calibrated to the 2MASS system, with errors in parentheses.

Date	MJD	<i>J</i>	<i>H</i>	<i>K</i>	Instrument
20120111	55937.23	14.15 (0.16)	13.72 (0.17)	13.55 (0.18)	REMIR
20120112	55938.29	14.14 (0.15)	13.71 (0.30)	13.55 (0.26)	REMIR
20120113	55939.35	13.61 (0.16)	13.89 (0.17)	13.44 (0.33)	REMIR
20120124	55950.26	13.43 (0.32)	13.38 (0.26)	13.31 (0.39)	REMIR
20120211	55968.12	13.38 (0.11)	13.04 (0.14)	13.35 (0.13)	REMIR
20120216	55973.29	13.37 (0.46)	13.09 (0.40)	13.22 (0.32)	REMIR
20120225	55982.08	13.28 (0.29)	12.97 (0.23)	12.98 (0.28)	REMIR
20120305	55991.09	13.67 (0.17)	13.66 (0.19)	13.29 (0.39)	REMIR
20120314	56000.08	13.56 (0.12)	13.34 (0.17)	13.30 (0.28)	SOFI
20120315	56001.18	13.68 (0.25)	13.31 (0.16)	13.15 (0.14)	SOFI
20120325	56011.01	13.83 (0.18)	13.32 (0.06)	13.47 (0.14)	REMIR
20120405	56022.11	13.78 (0.04)	13.70 (0.06)	13.65 (0.20)	REMIR
20120412	56029.11	14.18 (0.19)	13.92 (0.08)	14.11 (0.16)	REMIR
20120416	56033.10	14.34 (0.23)	14.01 (0.07)	14.14 (0.08)	REMIR
20120421	56038.10	14.66 (0.07)	14.47 (0.10)	14.30 (0.14)	REMIR
20120507	56054.00	15.35 (0.29)	14.93 (0.12)	14.91 (0.16)	NOTCAM

**Figure 2.** Light curves of SN 2012A in *UBVR IJHK* bands. The insert is a zoom on the early *R*-band light curve.

ter combinations as a function of the light curve phase. The difference between the observed magnitudes (filled circles) is compared with the expected difference (empty circles) as derived from the transformation equations of Chonis & Gaskell (2008) using the observed  $g - r$  and  $r - i$  colours.

Besides the *AB - VEGA* systematic offset, Figure 4 shows in all bands apart from  $r - R$  a clear trend with phase. This is largely expected because of the rapid SN colour evolution and dependence of the transformation equation on the colour. Indeed it appears that the transformation equations are a fairly good approximation for the  $g - V$  and  $r - R$  differences, but less valid for the  $g - B$  and  $i - I$  differences. While the differences in  $g - B$  are readily attributed to the very different passbands of the two filters resulting in a different sampling of the evolving spectral energy distribution of the SN, the large systematic offset in  $i - I$  required fur-

ther analysis. It transpired that the *i* filter of PROMPT has a somewhat redder cutoff than the SDSS *i* filter and hence it includes the strong Ca II feature at  $\sim 8600 \text{ \AA}$  that is outside of the SDSS *i* band. This effect accounts for the offset of  $\sim 0.15$  mag of the observed differences and those expected from the transformation equations.

We conclude that provided filters are carefully matched, transformation equations can be safely used for SNe IIP, apart from for  $g - B$ .

### 3.3 Distance and absolute magnitudes

The *Nearby Galaxies Catalog* by Tully (1988) reports for NGC 3239 a distance of 8.1 Mpc, based on the measured redshift and using a model for the local velocity field. Indeed, as is well known, the redshift of nearby galaxies is perturbed by the influence of the Virgo cluster, the Great Attractor (GA), and the Shapley supercluster. It turns out that updated models of the local velocity field yield a distance that is about 20% larger than the above value, that is  $9.8 \pm 0.7$  Mpc as also reported by the NASA/IPAC Extragalactic database (NED)<sup>3</sup>. This is fully consistent with the value of 10.0 Mpc reported in the *Extragalactic Distance Database* (Tully et al. 2009) and obtained with the same method. In the following we adopt a distance of 9.8 Mpc, i.e. a distance modulus of 29.96 mag with a formal error of 0.15 mag as reported by NED ( $H_0 = 73 \text{ km s}^{-1} \text{ Mpc}^{-1}$ ). We also derive the total extinction in the direction of NGC 3239 (Galactic plus host galaxy) as  $A_B = 0.15$  mag (see Section 4.4).

The SN apparent magnitudes at maximum were estimated through a low order polynomial fit of the early light curves ( $< 30$  d), from which we obtained  $m_B = 13.98 \pm 0.03$  mag,  $m_V = 13.81 \pm 0.03$  mag and  $m_R = 13.66 \pm 0.03$  mag, where the error budget is dominated by the fact that, with the exception of the *R*-band, the rise to the maximum light

<sup>3</sup> <http://ned.ipac.caltech.edu>

**Table 6.** Photometry in *griz* bands. The magnitude system is as for SDSS DR7, that is  $SDSS = AB - 0.02$  mag. Errors are given in parentheses.

Date	MJD	<i>g</i>	<i>r</i>	<i>i</i>	<i>z</i>	Instrument
20120113	55939.25	14.04 ( 0.10)	13.88 ( 0.07)	14.12 ( 0.05)	14.30 ( 0.05)	PROMPT
20120114	55940.27	14.13 ( 0.07)	13.90 ( 0.10)	14.17 ( 0.07)	14.23 ( 0.05)	PROMPT
20120118	55944.21	14.07 ( 0.07)	13.90 ( 0.04)	14.06 ( 0.04)	14.25 ( 0.10)	PROMPT
20120121	55947.23	14.16 ( 0.08)	13.86 ( 0.08)	14.01 ( 0.06)	14.15 ( 0.08)	PROMPT
20120125	55951.22	14.23 ( 0.22)				PROMPT
20120126	55952.24		13.95 ( 0.05)	14.03 ( 0.10)	14.16 ( 0.10)	PROMPT
20120131	55957.21	14.45 ( 0.07)	14.09 ( 0.06)	14.13 ( 0.08)	14.01 ( 0.07)	PROMPT
20120209	55966.20	14.86 ( 0.03)	14.02 ( 0.04)	14.22 ( 0.06)	14.01 ( 0.06)	PROMPT
20120214	55971.18	14.78 ( 0.06)	14.06 ( 0.03)	14.11 ( 0.07)	14.14 ( 0.09)	PROMPT
20120217	55974.18	14.82 ( 0.07)	14.07 ( 0.04)	14.15 ( 0.06)	14.03 ( 0.04)	PROMPT
20120221	55978.32		14.14 ( 0.04)	14.18 ( 0.07)	14.14 ( 0.07)	PROMPT
20120224	55981.17		14.20 ( 0.06)	14.15 ( 0.06)	14.13 ( 0.07)	PROMPT
20120227	55984.15	14.95 ( 0.07)	14.14 ( 0.06)	14.26 ( 0.10)	13.99 ( 0.08)	PROMPT
20120229	55986.14	14.96 ( 0.27)				PROMPT
20120301	55987.14		14.26 ( 0.05)	14.21 ( 0.04)	14.19 ( 0.06)	PROMPT
20120304	55990.13	15.06 ( 0.05)	14.11 ( 0.05)	14.24 ( 0.05)	14.05 ( 0.06)	PROMPT
20120312	55998.12	15.17 ( 0.06)	14.27 ( 0.04)	14.36 ( 0.07)	14.12 ( 0.06)	PROMPT
20120314	56000.11	15.17 ( 0.10)	14.27 ( 0.04)	14.32 ( 0.07)	14.13 ( 0.06)	PROMPT
20120316	56002.07	15.06 ( 0.28)				PROMPT
20120317	56003.05		14.40 ( 0.05)	14.44 ( 0.06)	14.24 ( 0.11)	PROMPT
20120319	56005.12	15.22 ( 0.08)	14.35 ( 0.03)	14.36 ( 0.04)	14.25 ( 0.05)	PROMPT
20120322	56008.12	15.29 ( 0.09)	14.39 ( 0.06)	14.41 ( 0.04)	14.30 ( 0.05)	PROMPT
20120324	56010.08	15.30 ( 0.09)	14.42 ( 0.04)	14.50 ( 0.05)	14.34 ( 0.10)	PROMPT
20120326	56012.10	15.26 ( 0.27)				PROMPT
20120327	56013.04		14.57 ( 0.06)	14.58 ( 0.08)	14.48 ( 0.07)	PROMPT
20120330	56016.07	15.42 ( 0.08)	14.56 ( 0.05)	14.63 ( 0.07)	14.51 ( 0.06)	PROMPT
20120403	56020.06	15.53 ( 0.09)	14.61 ( 0.05)	14.74 ( 0.10)	14.53 ( 0.09)	PROMPT
20120409	56026.13	15.61 ( 0.06)	14.82 ( 0.05)	14.96 ( 0.08)	14.64 ( 0.13)	PROMPT
20120412	56029.11		14.97 ( 0.04)	15.07 ( 0.04)	14.79 ( 0.11)	PROMPT
20120415	56032.13		15.10 ( 0.07)	15.16 ( 0.07)	14.94 ( 0.09)	PROMPT
20120417	56034.15		15.19 ( 0.06)	15.28 ( 0.05)	15.05 ( 0.10)	PROMPT
20120419	56036.04	16.45 ( 0.07)	15.34 ( 0.04)	15.46 ( 0.08)	15.21 ( 0.08)	PROMPT
20120422	56039.04	16.89 ( 0.09)	15.72 ( 0.09)	15.79 ( 0.05)	15.42 ( 0.22)	PROMPT

is not really well constrained. Keeping in mind this uncertainty in the detection of maximum epoch, we derived SN absolute magnitudes at maximum of  $M_B = -16.23 \pm 0.16$  mag,  $M_V = -16.28 \pm 0.16$  mag,  $M_R = -16.41 \pm 0.16$  mag, close to the average for SNe IIP (Li et al. 2011). In particular at maximum SN 2012A was very similar to SN 1999em which had  $M_B = -16.1 \pm 0.4$  mag (with a relatively large uncertainty in the host galaxy distance) and about 1 mag brighter than the faint type IIP SN 2005cs with  $M_B = -15.1 \pm 0.3$  mag.

We can use the Nugent et al. (2006) correlation between the absolute brightness of SNe IIP and the expansion velocities derived from the minimum of the Fe II 5169 Å P-Cygni feature observed during the plateau phase. Incorporating our  $V - I$  colour and the velocity measured from the Fe II 5169 Å line at +50 d in equation (1) of Nugent et al. (2006), we find a distance modulus of  $29.72 \pm 0.17$  mag which, within the uncertainties, is consistent with the assumed value.

### 3.4 Bolometric light curve

By integrating the multicolour photometry of SN 2012A from the *UV* to the near *IR*, we can derive the bolometric luminosity. In practice, for each epoch and filter, we derived the flux at the effective wavelength. When no observation in a given filter/epoch was available, the missing measurement was obtained through interpolation of the light curve in the given filter or, if necessary, by extrapolating the missing photometry assuming a constant colour from the closest available epoch. The fluxes, corrected for extinction, provide the spectral energy distribution at each epoch, which is integrated by the trapezoidal rule, assuming zero flux at the integration boundaries. The observed flux is converted into luminosity for the adopted distance.

We note that, shortly after discovery, the SN was not detected in radio setting a fairly restrictive upper limit to the radio luminosity (Stockdale et al. 2012) and that the *X*-ray detection, even neglecting the probable contamination by nearby sources, corresponds to a negligible contribution to the bolometric flux of about  $1 \times 10^{39}$  erg s<sup>-1</sup> (?), that is < 1% of the bolometric flux in the first month after explosion.

The bolometric light curve is presented in Figure 5 to-

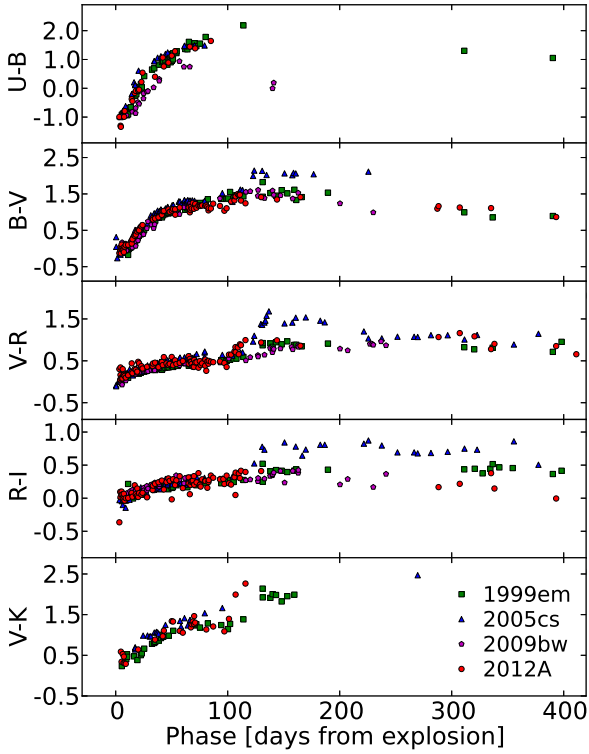


**Figure 3.** From the top to the bottom:  $U - B$ ,  $B - V$ ,  $V - R$ ,  $R - I$ ,  $V - K$  colours of SN 2012A from early times to the nebular phase, compared to SNe 2005cs, 1999em and 2009bw (see text for discussion).

gether with those of SNe 1999em, 2005cs and 2009bw computed with the same prescription. SN 1999em was selected as reference because it provided the best match with the early spectrum of SN 2012A as given by the automatic classification tool (cf. Section 2), while SNe 2005cs and 2009bw were chosen because they appear to encompass the observed properties of SN 2012A being fainter and brighter than SN 2012A, respectively. In fact it appears that the early luminosity of SN 2012A well matches that of SN 1999em.

We emphasize that at very early phases the far  $UV$  spectral range contributes almost 50% of the total bolometric luminosity, but in two weeks it drops to less than 10%. This should be taken into account when comparing with other SNe without far  $UV$  coverage.

As noted before, in SN 2012A the *plateau* luminosity is not really constant showing a monotonic decline up to 80 – 90 days from explosion. The drop, marking the end of the hydrogen envelope recombination, begins 15 – 20 days earlier than in most type IIP SNe, including SNe 1999em and 2005cs, and the late linear tail sets in earlier. Also we note that in SN 2012A the drop in luminosity from the plateau to the light curve tail is deeper than in SNe 1999em or 2005cs and similar to SN 2009bw. Moreover the luminosity of the linear late tail is intermediate between those of SNe 1999em and 2005cs, resembling SN 2009bw. As mentioned previously, in typical type II SNe the linear tail is powered by

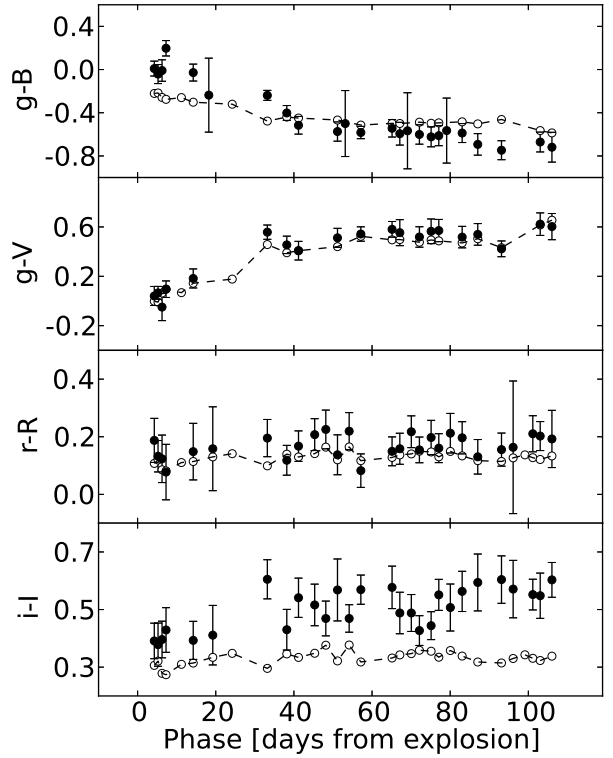


**Figure 4.** Comparison between *griz* and Johnson-Cousins photometry for SN 2012A. The differences between the observed magnitudes (filled circles) is compared with the expected differences (empty circles) as derived from the transformation equations of Chonis & Gaskell (2008), see text for discussion.

the energy input from  $^{56}\text{Co}$  decay. This is confirmed by the observed luminosity decline rate of SN 2012A that, as seen in Figure 5, matches fairly well the predicted decline assuming that all the high energy photons and positrons from the radioactive decay are fully trapped and converted into  $UV$ -optical radiation. In this case, the tail luminosity is a direct indicator of the amount of  $^{56}\text{Ni}$  (the parent element in the radioactive chain) produced in the explosion. We can therefore conclude that the  $^{56}\text{Ni}$  mass of SN 2012A was about half that of SN 1999em and about twice that of SN 2005cs.

For a more accurate determination of the  $^{56}\text{Ni}$  mass it is convenient to refer to SN 1987A for which the mass of radioactive nickel has been accurately estimated to be  $M(^{56}\text{Ni}) = 0.075 \pm 0.005 M_{\odot}$  (Danziger 1988; Woosley, Hartmann, & Pinto 1989). The comparison of the bolometric light curves of SNe 2012A and 1987A, computed integrating the luminosity in the same spectral range, shows that  $L(2012A)/L(1987A) = 0.14$  from which we derive  $M(^{56}\text{Ni}) = 0.011 \pm 0.004 M_{\odot}$  for SN 2012A, where the error budget is dominated by the uncertainty on the distance.

As an independent check, following Elmhamdi, Chugai, & Danziger (2003b), we estimated the steepness function  $S$ , defined as steepness of the  $V$  light curve at the inflection point during the rapid drop from

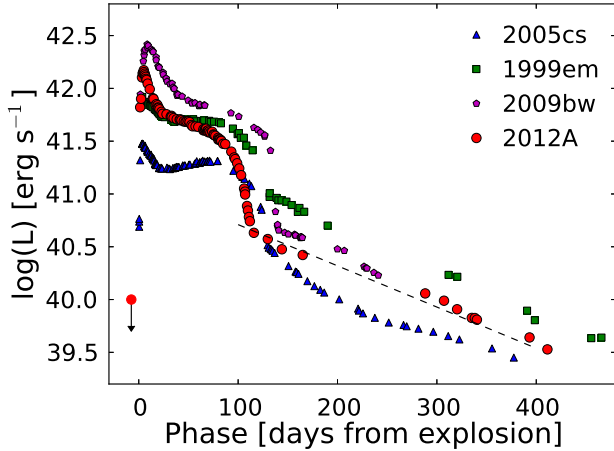


**Figure 5.** Bolometric light curve of SN 2012A, computed integrating the fluxes from the *UV* to near *IR* bands, compared with those of the type IIP SNe 2005cs, 1999em and 2009bw. The dashed line shows the slope of the  $^{56}\text{Co}$  decay.

the plateau to the radioactive tail. It was shown that  $S$  is strongly correlated to the ejected  $^{56}\text{Ni}$  mass (cf. Figure 5 in Elmhamdi, Chugai, & Danziger 2003b). From a value of  $S = 0.16 \text{ mag d}^{-1}$  for SN 2012A, we calculate  $M(^{56}\text{Ni}) = 0.015 M_{\odot}$ , which is in good agreement with the value derived from the observed luminosity in the radioactive tail.

The ejected mass of  $^{56}\text{Ni}$  derived for SN 2012A is intermediate between those of prototypical SNe IIP, e.g. SNe 1969L and 1988A for which  $M(^{56}\text{Ni}) = 0.07 M_{\odot}$  (Turatto et al. 1993), and the value for underluminous SNe IIP (Pastorello et al. 2004), e.g. SNe 1997D and 2005cs, for which  $M(^{56}\text{Ni}) = 0.002 M_{\odot}$  and  $0.003 M_{\odot}$ , respectively (Turatto et al. 1998; Benetti et al. 2001; Pastorello et al. 2009). A similar  $^{56}\text{Ni}$  mass was found for SN 2009bw [ $M(^{56}\text{Ni}) = 0.022 M_{\odot}$ , cf. Inserra et al. (2012)].

## 4 SPECTROSCOPY

Spectroscopic observations of SN 2012A were carried out with several telescopes commencing short after explosion, continued for well over one year, and yielding a total of 47 epochs of medium/low resolution spectroscopy. In addition, high-resolution spectra were obtained at four epochs. The journal of the spectroscopic observations is given in Table 7. For each spectrum we report: the date, MJD and phase from explosion, the telescope and the instrumental configuration, the spectral range and, finally, the resolution, estimated from the FWHM of the night sky lines.

Data reduction was performed using standard IRAF tasks. Spectral images were bias and flat-field corrected, before the SN spectrum was extracted by tracing the stellar profile along the spectral direction and subtracting the sky background along the slit direction. Wavelength calibration was accomplished by obtaining comparison lamp spectra, while for flux calibration we referred to the observations of spectrophotometric standard stars obtained, when possible, in the same nights as the SN. The flux calibration of all spectra was verified against *BVRI* photometry and cor-

rected, if necessary. The telluric absorption corrections were estimated from the spectra of spectrophotometric standards. Notwithstanding this, often imperfect removal can affect the profile of the SN features that overlap with the strongest atmospheric absorptions, in particular the telluric band at  $7570 - 7750 \text{ \AA}$ .

For the high-resolution spectra we performed an additional check on the accuracy of the wavelength calibration by measuring the wavelength of night-sky lines (O I, OH, Hg I and Na I D, Osterbrock et al. 2000). With this we achieved an accuracy of the velocity scale of  $0.1 \text{ km s}^{-1}$ .

### 4.1 Spectral evolution

The overall spectral evolution of SN 2012A is shown in Figures 6 and 7. The first set of spectra (Figure 6) illustrates the spectral evolution during the hydrogen envelope recombination from shortly after shock breakout (+3 d) to the beginning of the transition phase, while the second set (Figure 7) shows the transition from the photospheric to the nebular phase.

The earlier spectra are characterized by a very blue continuum, with blackbody temperatures above  $10^4 \text{ K}$ . The only prominent features are the hydrogen Balmer lines with broad P-Cygni profiles, and He I  $5876 \text{ \AA}$ . After a couple of weeks, the He I  $5876 \text{ \AA}$  disappears while the metal lines increase in strength, and after one month, become the dominant features (apart from  $\text{H}\alpha$  and  $\text{H}\beta$ ). The identified lines include Fe II ( $4500 \text{ \AA}$ ,  $4924$ ,  $5018$  and  $5169 \text{ \AA}$ ), Sc II ( $4670 \text{ \AA}$ ,  $5031 \text{ \AA}$ ), Ba II ( $6142 \text{ \AA}$ ), Ca II ( $8498$ ,  $8542$  and  $8662 \text{ \AA}$ , H&K), Ti II (blended with Ca II H&K). Strong line blanketing, especially by Fe II transitions, characterizes the blue spectral region below  $3800 \text{ \AA}$ , suppressing much of the *UV* flux. The Na I D feature emerges where earlier on He I  $5876 \text{ \AA}$  was detected.

In the spectra between +10 to +25 d, a faint absorption feature is visible at about  $6270 \text{ \AA}$ , just to the blue side of the  $\text{H}\alpha$  P-Cygni absorption. A similar feature was detected by Pastorello et al. (2006) in SN 2005cs and attributed either to high-velocity detached hydrogen (for SN 2012A  $\sim 13800 \text{ km s}^{-1}$ ) or to the Si II  $6347 - 6371 \text{ \AA}$  doublet. The lack of a similar absorption feature in the blue side of  $\text{H}\beta$  (left and middle panels of Figure 8) supports the Si II identification. In this case, adopting for the Si II doublet an effective wavelength of  $6355 \text{ \AA}$ , the expansion velocity as measured by fitting the P-Cygni absorption profile would be  $\sim 4400 \text{ km s}^{-1}$  around +12 d, and decreases to  $4000 \text{ km s}^{-1}$  in the following epochs. These expansion velocities are comparable to those derived from Fe II  $5169 \text{ \AA}$  at similar phases (cf. Figure 12).

The evolution of  $\text{H}\alpha$  from +109 to +173 d is shown in the right panel of Figure 8. While within 100 days from explosion  $\text{H}\alpha$  was characterized by a symmetric P-Cygni profile, by day 109 – 112 a double peaked emission starts to develop and becomes more evident in the subsequent spectra at phases 116 – 154 d. A complex profile is seen in  $\text{H}\beta$  as well, even though the blend of several lines prevents the recognition of multiple components there.  $\text{H}\alpha$  asymmetry was observed before in SN 1987A (Phillips & Williams 1991; Chugai 1991), SN 1999em (Elmhamdi et al. 2003a) and SN 2004dj (Chugai et al. 2005). For the first two SNe an asymmetric, redshifted  $\text{H}\alpha$  line was reported, while SN

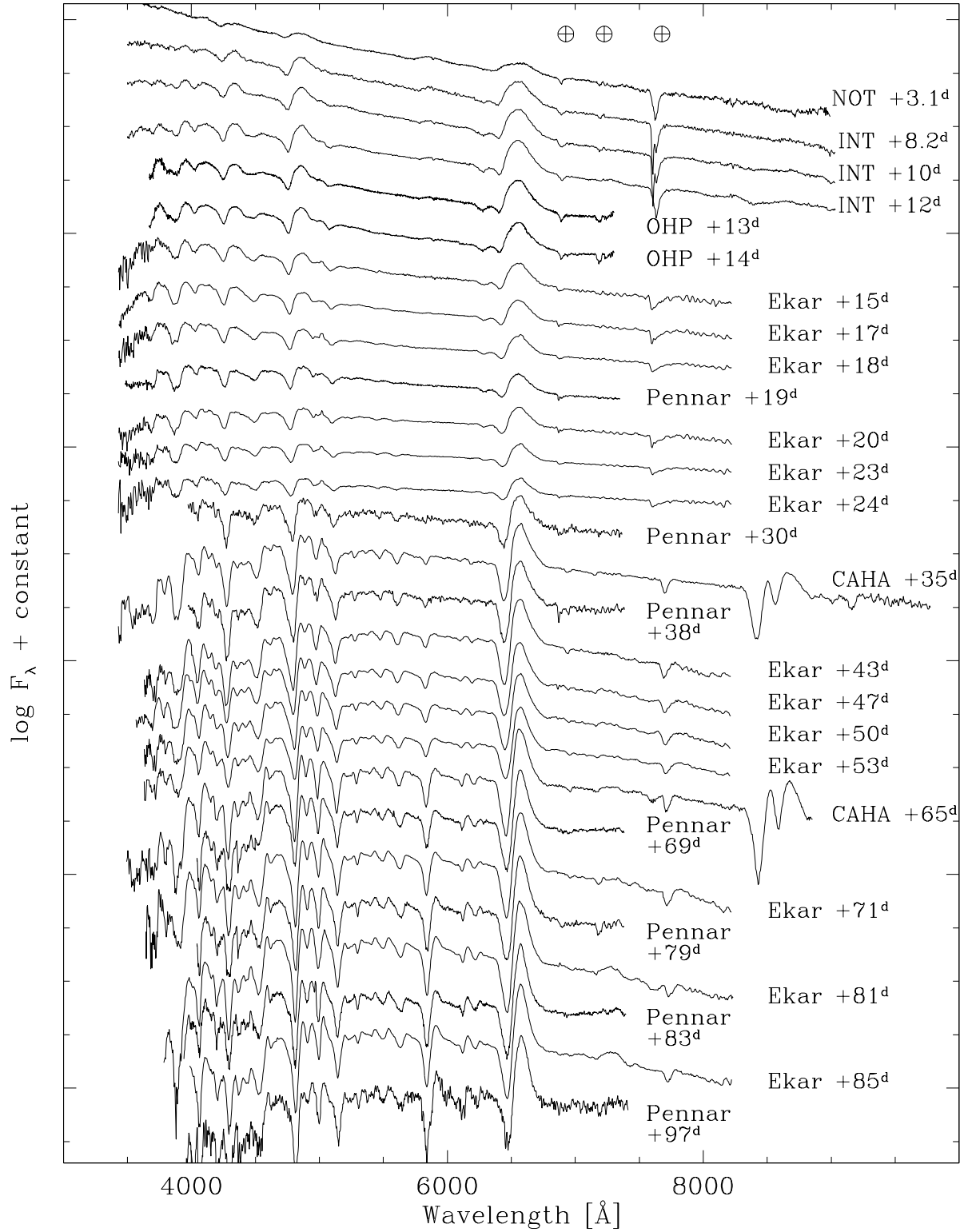


**Figure 6.** SN 2012A: spectral evolution during the first 3 months. See Table 7 for the reference to the telescopes labeled in the figure and the instrumental configuration. Wavelength is in the observed frame, telluric absorptions are marked with a  $\oplus$  symbol. The NTT SOFI+EFOSC2 spectrum at phase +67 d (3350–25000  $\text{\AA}$ ) is shown in Figure 9.

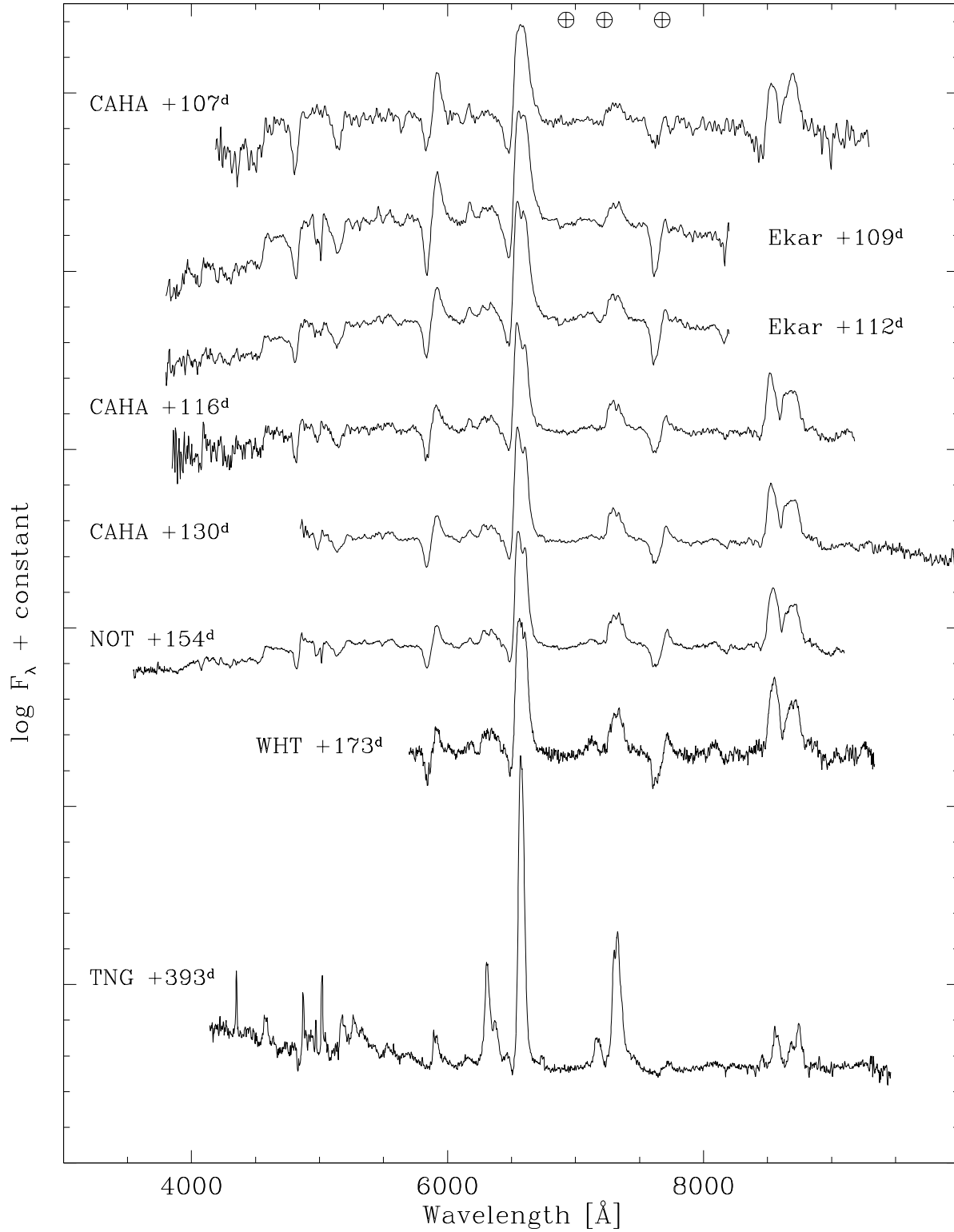


**Figure 7.** SN 2012A: spectral evolution during the nebular phase. See Table 7 for the reference to the telescopes labeled in the figure and the instrumental configuration. Wavelength is in the observed frame, telluric absorptions are marked with a  $\oplus$  symbol.

**Table 7.** Journal of spectroscopic observations. Phase is from the adopted epoch of explosion,  $\text{MJD}=55933_{-3}^{+1}$ 

Date	MJD	Phase [d]	Instrumental configuration <sup>1</sup>	Range [Å]	Resolution [Å]
20120109	55936.14	3.1	NOT+ALFOSC+gm4	3400-9000	14
20120110	55936.95	3.9	Ekar+Echelle+gr300	3780-7400	0.34
20120115	55941.08	8.1	Ekar+Echelle+gr300	4060-7785	0.38
20120115	55941.21	8.2	INT+IDS+R150V	3500-10000	13
20120116	55942.14	9.1	Ekar+Echelle+gr300	4060-7785	0.38
20120117	55943.14	10.1	INT+IDS+R150V	3500-10000	13
20120117	55943.97	11.0	OHP+1.93m+Carelec	3700-7300	7
20120118	55944.03	11.0	Ekar+AFOSC+gm4,gm2	3500-9200	24
20120118	55944.14	11.1	INT+IDS+R150V	3500-10000	13
20120118	55944.98	12.0	OHP+1.93m+Carelec	3700-7300	7
20120119	55945.19	12.2	INT+IDS+R150V	3500-10000	13
20120120	55946.06	13.1	OHP+1.93m+Carelec	3700-7300	7
20120121	55947.00	14.0	OHP+1.93m+Carelec	3700-7300	7
20120121	55947.98	15.0	Ekar+AFOSC+gm4	3500-8200	24
20120123	55949.98	17.0	Ekar+AFOSC+gm4	3500-8200	24
20120124	55950.97	18.0	Ekar+AFOSC+gm4	3500-8200	24
20120126	55952.15	19.1	Pennar+B&C+300tr/mm	3400-7800	10
20120127	55953.03	20.0	Ekar+AFOSC+gm4	3500-8200	24
20120129	55955.97	22.9	Ekar+AFOSC+gm4	3500-8200	24
20120130	55956.92	23.9	Ekar+AFOSC+gm4	3500-8200	24
20120205	55962.94	29.9	Pennar+B&C+300tr/mm	3400-7800	10
20120210	55968.11	35.1	CAHA+CAFOS+b200+r200	3400-10500	10
20120213	55970.94	37.9	Pennar+B&C+300tr/mm	3400-7800	10
20120218	55975.94	42.9	Ekar+AFOSC+gm4	3500-8200	24
20120222	55980.00	47.0	Ekar+AFOSC+gm4	3500-8200	24
20120225	55982.99	50.0	Ekar+AFOSC+gm4	3500-8200	24
20120228	55985.92	52.9	Ekar+AFOSC+gm4	3500-8200	24
20120306	55992.88	59.9	Pennar+B&C+300tr/mm	3400-7800	10
20120309	55996.43	63.4	Ekar+Echelle+gr300	3780-7400	0.34
20120311	55998.09	65.1	CAHA+CAFOS+b200	3300-8850	13
20120313	55999.18	66.2	NTT+EFOSC2+gr11+gr16	3350-10000	12
20120315	56000.11	67.1	NTT+SOFI+GB+GR	9400-25000	20
20120315	56001.88	68.9	Pennar+B&C+300tr/mm	3400-7800	10
20120317	56003.91	70.9	Ekar+AFOSC+gm4	3500-8200	24
20120325	56012.01	79.0	Pennar+B&C+300tr/mm	3400-7800	10
20120327	56013.84	80.8	Ekar+AFOSC+gm4	3500-8200	24
20120329	56015.83	82.8	Pennar+B&C+300tr/mm	3400-7800	10
20120331	56017.90	84.9	Ekar+AFOSC+gm4	3500-8200	24
20120412	56029.82	96.8	Pennar+B&C+300tr/mm	3400-7800	10
20120422	56040.06	107.1	CAHA+CAFOS+g200	4100-10200	13
20120424	56041.91	108.9	Ekar+AFOSC+gm4	3500-8200	24
20120427	56044.94	111.9	Ekar+AFOSC+gm4	3500-8200	24
20120501	56048.89	115.9	CAHA+CAFOS+g200	3800-10200	13
20120515	56062.87	129.9	CAHA+CAFOS+g200	3800-10200	13
20120515	56062.89	129.9	INT+IDS+R150V	4000-9500	10
20120608	56086.89	153.9	NOT+ALFOSC+gm4	3400-9000	14
20120627	56105.89	172.9	WHT+ISIS+R300B+R158R	3500-10000	5
20130203	56326.05	393.1	TNG+LRS+LR-B,LR-R	3350-10370	10

<sup>1</sup> NOT = 2.56m Nordic Optical Telescope (La Palma, Spain); Ekar = Copernico 1.82m Telescope (Mt. Ekar, Asiago, Italy); INT = 2.5m Isaac Newton Telescope (La Palma, Spain); OHP = Observatoire de Haute-Provence 1.93m Telescope (France); Pennar = Galileo 1.22m Telescope (Pennar, Asiago, Italy); CAHA = Calar Alto Observatory 2.2m Telescope (Andalucia, Spain); NTT = 3.6m ESO NTT (La Silla, Chile); WHT = 4.2m William Herschel Telescope (La Palma, Spain); TNG = 3.6m Telescopio Nazionale Galileo (La Palma, Spain).

2004dj showed a double peaked structure. A similar H $\alpha$  profile clearly arises in SN 2012A by day +112, with a dominant blue peak shifted by  $\sim -1000 \text{ km s}^{-1}$  and a red one shifted by  $\sim +1300 \text{ km s}^{-1}$ . As suggested by Chugai et al. (2005) and Chugai (2006) for SN 2004dj, this may indicate an asymmetric (bipolar) ejection of  $^{56}\text{Ni}$  in the otherwise spherically-

symmetric envelope. Moreover, as for SN 2004dj, the prominence of the blue peak over the red one can be explained with a  $^{56}\text{Ni}$  distribution that is skewed towards the observer. In the following spectra of SN 2012A, the H $\alpha$  profile shows some evolution, with the blue peak receding to  $-500 \text{ km s}^{-1}$  and the red peak increasing to  $\sim +1800 \text{ km s}^{-1}$ . Finally, in

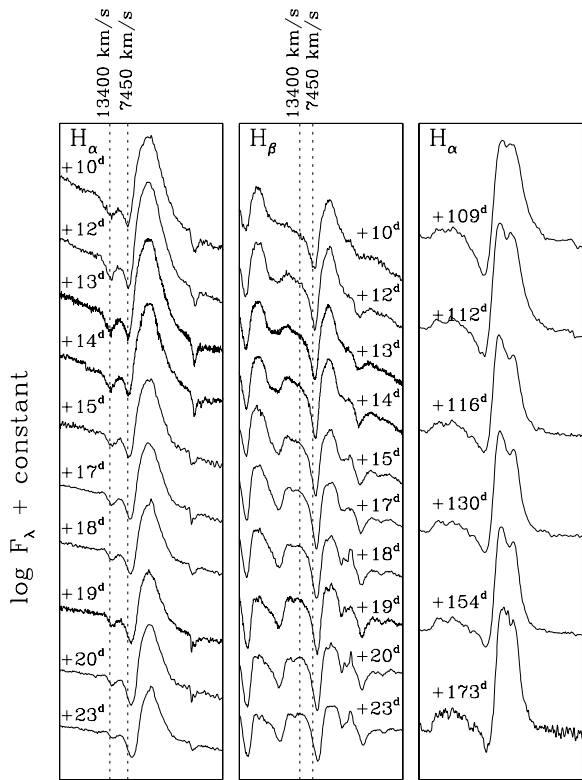


**Figure 8.** Evolution of the Balmer lines in SN 2012A. Left panel: evolution of  $H\alpha$  during the early photospheric phase; the two dashed lines correspond to the minimum of the P-Cygni profile of the spectrum at +10 d ( $\sim 7450 \text{ km s}^{-1}$ ) and to the faint absorption just to the blue of the  $H\alpha$  P-Cygni absorption ( $\sim 13400 \text{ km s}^{-1}$  if identified with  $H\alpha$ ). Middle panel: the same as in the left panel but for  $H\beta$  where there is no evidence of a similar absorption feature. Right panel: evolution of the  $H\alpha$  profile during the transition from the photospheric to the nebular phase. We emphasize the asymmetry of the  $H\alpha$  emission.

the late nebular spectrum (+394 d, see Figure 7),  $H\alpha$  shows a single narrow Gaussian profile. We note that the [Ca II] 7391, 7324 Å features seem to show a similar structure, although we cannot test with the [O I] doublet (6300, 6364 Å) as this line becomes prominent only in our last spectrum at phase +394 d.

In Figure 9 we compare the spectra of SN 2012A at about maximum, one month and one year after explosion with those of SN 1999em (Elmhamdi et al. 2003a) and SN 2005cs (Pastorello et al. 2006) taken at comparable phases. Several similarities with these SNe IIP, and in particular with SN 1999em, have already been remarked upon. All CC SNe are characterized by blue continua at the early phases with blackbody temperatures that become very similar after about one month. These three SNe also show similar spectral features, with Balmer lines and He I 5876 Å early on, and one month later the emergence of metal lines, in particular Fe II, Sc II, Ba II and the Ca II infrared triplet.

During the transition from the plateau to the radioactive tail (Figure 7), the continuum emission remains strong. This can be seen from the deep absorption of Na I and a new strong feature of O I at 7774 Å. At the same time nebular emission lines begin to emerge, first of all [Ca II] 7291, 7324 Å and subsequently [O I] 6300, 6364 Å and [Fe II]

7155, 7171 Å. The last spectrum taken at +394 d is well in the nebular phase. Along with the always strong  $H\alpha$  line, with  $\text{FWHM} \simeq 2000 \text{ km s}^{-1}$ , the most prominent lines are permitted emissions from  $H\beta$ , Na I D and the Ca II infrared triplet and forbidden lines of [Ca II], [O I], [Fe II] and Mg I] 4572 Å. Additional emission in the range 5000 – 5500 Å and around 7710 Å is most likely due to [Fe I] and [Fe II] multiplets. We also notice that bluewards of 4500 Å, the spectrum shows the signature of a blue continuum that most likely is due to contamination from a nearby hot star or association.

In Table 8 we report the measurements of the flux of the most prominent lines detected in the latest spectrum. Nebular line fluxes for a sample of SNe IIP have been collected by Maguire et al. (2012) showing only a moderate variation from object to object. Actually, for SN 2012A the Ca II and O I emission relative to  $H\alpha$  are among the weakest of the sample for the given phase, whereas the Fe II/ $H\alpha$  emission ratio is close to the average. The ratio of the two lines in the [O I] 6300, 6364 doublet is 2.6, similar to SN 2004et and close to the expected value for the thin regime, whereas for most SNe II at this phase the ratio is much lower signaling that the ejecta still has some optical depth.

Jerkstrand et al. (2012) have used their spectral synthesis code to model the nebular emission line fluxes for SN explosions of different mass progenitors, and find [O I], Na I D and Mg I] to be the most sensitive lines. By comparing their models with late time observations of the type IIP SN 2004et, they found a best match with a  $15 M_{\odot}$  progenitor model. From Table 8 we derive the fractions of the line luminosities normalized to the luminosity from the  $^{56}\text{Co}$  decay at +394 days (assuming  $M(^{56}\text{Ni}) = 0.011 M_{\odot}$  and a distance of 9.8 Mpc, cf. Sections 3.3, 3.4), finding values of 2.6% for [O I] 6300, 6364 Å, 0.70% for Na I D and 0.63% for Mg I] 4571 Å. The comparison with the expected line flux from models (see Figure 8 in Jerkstrand et al. 2012) shows that the [O I] and Na I D values are close to the  $15 M_{\odot}$  track, while the Mg I] line is closest to the  $19 M_{\odot}$  track. As discussed by Jerkstrand et al. (2012), the [O I] lines are more reliable mass indicators than the other ones. Therefore we conclude that the best match from the nebular spectrum analysis is for a  $15 M_{\odot}$  progenitor. However, we note that the nebular models in Jerkstrand et al. (2012) are computed for a higher mass of ejected  $^{56}\text{Ni}$  ( $M(^{56}\text{Ni}) = 0.062 M_{\odot}$  as derived for SN 2004et). A lower  $^{56}\text{Ni}$  mass will result in lower ionization and temperature, somewhat altering the fraction of cooling done by various emission lines.

Maguire et al. (2012) have also shown the existence of a correlation between Ni mass and ejecta expansion velocity, measured from the FWHM of the  $H\alpha$  line. By using this relation for SN 2012A we derive  $M(^{56}\text{Ni}) = 0.022^{+0.034}_{-0.013} M_{\odot}$  which, within the uncertainties is consistent with our measurement based on the late luminosity.

## 4.2 Near-infrared spectrum

A near infrared (NIR) spectrum of SN 2012A was collected with NTT+SOFI during the photospheric phase (+67 days), covering the wavelength region between 9400 to 25000 Å. It is shown in Figure 10 after merging with the +66 days optical spectrum taken with the same telescope but equipped with EFOSC2. This was compared with the NIR SN spectra presented in Gerardy et al. (2001); Fassia et al.

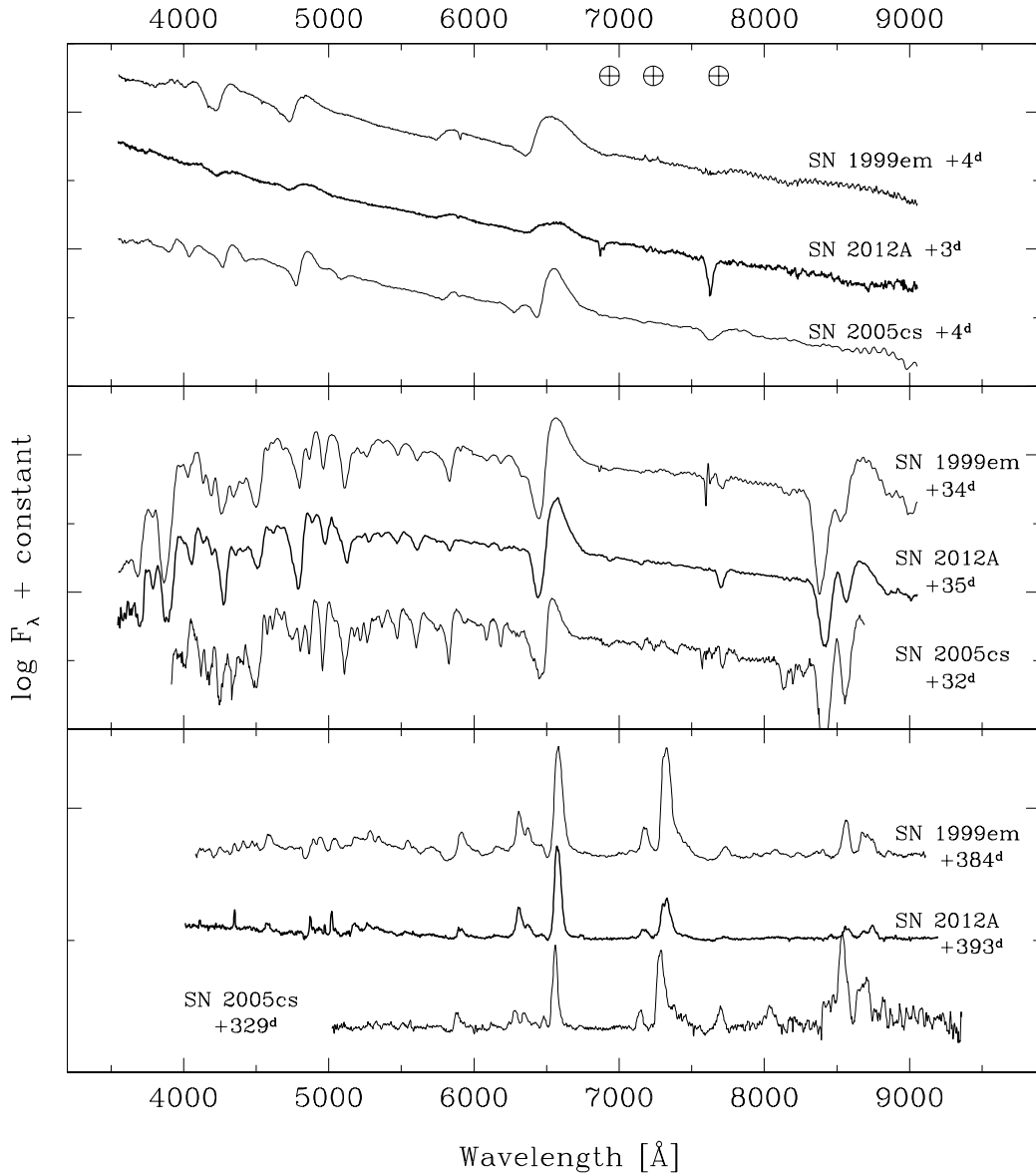


**Figure 9.** Comparison among spectra of SN 2012A, SN 1999em and SN 2005cs at similar phases. Top panel: few days past explosion; middle panel: about one month past explosion; bottom panel: about one year past explosion.

(2001); Pozzo et al. (2006) which were also used as guide for line identification. The NIR spectrum is dominated by the Paschen series of hydrogen, showing P-Cygni profiles similar to the Balmer lines.  $\text{Br}\gamma$  is also detected. In the insert of Figure 10 we show a zoomed-in-view of the NIR region between 9000 and 13000 Å. The spectral lines are typical of SNe IIP at this phase, in particular the blend of C I 10691 Å with He I 10830 Å that was also observed in coeval epochs are available, i.e. SN 1997D (Benetti et al. 2001), SN 1999em (Hamuy et al. 2001), SN 2005cs (Pastorello et al. 2009) and SN 2004et (Maguire et al. 2010b). Sr II 10327 Å is clearly visible, while the contribution of Fe II 10547 Å is not as evident as in other type II SNe (see for example SN 2005cs in Pastorello et al. 2009).

### 4.3 Blackbody temperature and expansion velocities

Estimates of the photospheric temperatures of SN 2012A were derived from blackbody functions fitted to the spectral continuum (the spectra were corrected for the redshift and adopted extinction), from a few days after explosion up to  $\sim 80$  days. Later on, due to both emerging emission lines and increased line blanketing which causes a flux deficit at the shorter wavelengths, the fitting of the continuum becomes difficult. The data are collected in Table 9, and the temperature evolution is shown in Figure 11, along with the same measurements for SNe 2005cs, 2009bw and 1999em for comparison. The errors were estimated from the dispersion of measurements obtained with different choices for the spectral fitting regions. The early photospheric temperature of SN 2012A is above  $1.2 \times 10^4$  K, but it decreases quickly

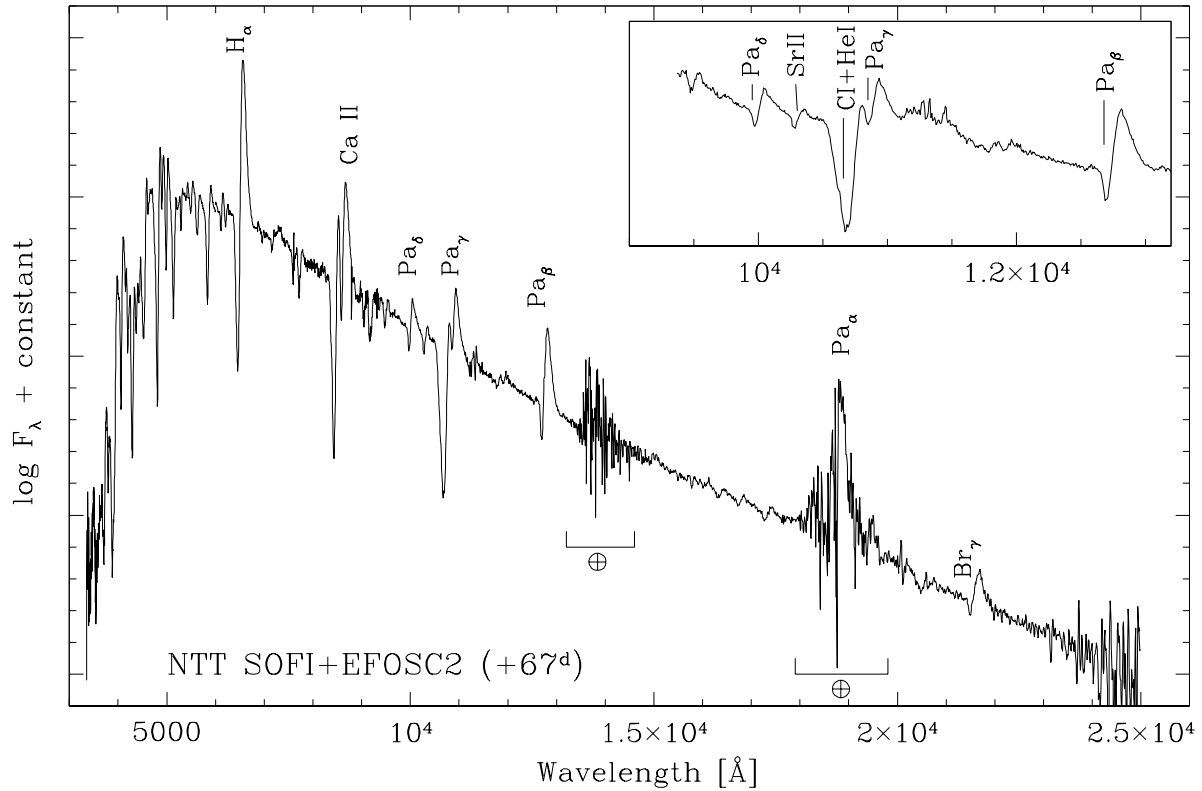


**Figure 10.** The spectrum of SN 2012A taken with ESO NTT, EFOSC2+SOFI at phase +67 days. The insert (top right-hand corner) shows a zoomed NIR region between 9000 – 13000 Å with identifications of the Paschen series, the blend of C I 10691 Å and He I 10830 Å, and Sr II 10327 Å.

**Table 8.** Flux measurements in the nebular spectrum at +394 d. The spectrum has been corrected for the adopted extinction in the direction of the SN 2012A,  $E(B - V) = 0.037$  mag.

Line	Flux [ $\times 10^{-14}$ erg cm $^{-2}$ s $^{-1}$ ]
H $\alpha$	4.10
[O I] 6300 Å	0.81
[O I] 6363 Å	0.31
[Fe II]	0.27
[Ca II]	1.90
Na I D	0.30
[Mg II]	0.27
Ca II NIR	1.00

to  $\sim 6000$  K within three weeks and then remains roughly constant. The evolution of SN 2012A is very similar to that of SNe 1999em and 2009bw, whereas SN 2005cs showed a much higher temperature at very early phases ( $2.9 \times 10^4$  K, Pastorello et al. 2006).

The expansion velocity of the ejecta is measured by fitting the P-Cygni absorption components of different lines, in particular H $\alpha$ , H $\beta$ , Fe II 5169 Å, Sc II 5527, 6245 Å, Ba II 6142 Å and He I 5876 Å. The latter is detected in the spectra during the first two weeks after core-collapse, while after about one month, Na I D emerges in the same spectral region. The expansion velocity evolution of the dif-

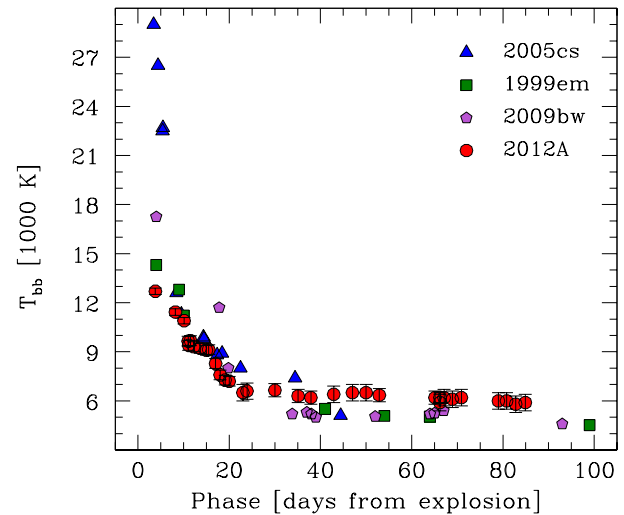


**Figure 11.** Evolution of the continuum temperature of SN 2012A and comparison with SNe 1999em, 2005cs and 2009bw.

ferent lines is shown Figure 12. H $\alpha$  displays systematically higher velocities than other lines, which is a consequence of the high optical depth of this transition. The comparison of the H $\alpha$  expansion velocity with that of other SNe II in Figure 13 shows once more that SN 2012A is more similar to SNe 1999em and 2009bw, whereas SN 2005cs has a much smaller velocity.

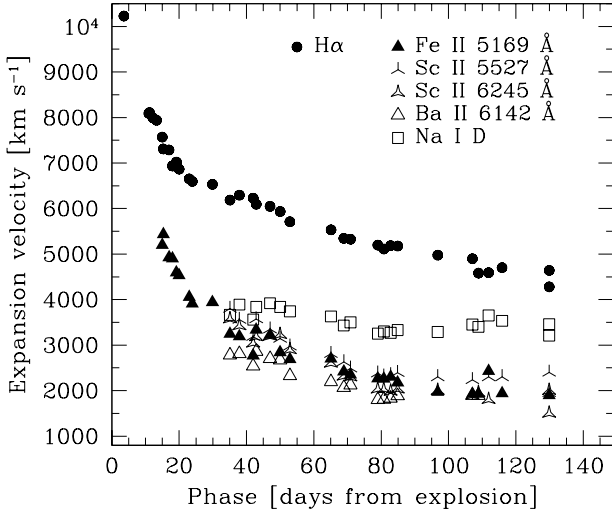


**Figure 12.** Expansion velocity of  $H\alpha$ , Na I D, Fe II 5169 Å, Sc II 5527, 6246 Å, and Ba II 6142 Å measured from the minima of P-Cygni profiles in the spectra of SN 2012A.

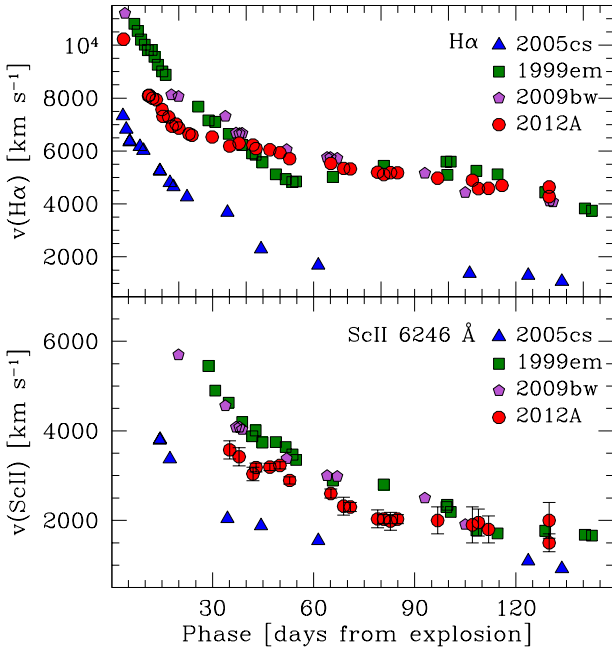


**Figure 13.** Expansion velocities of  $H\alpha$  (top panel) and Sc II 6246 Å (bottom panel) deduced from the minima of P-Cygni profiles in the spectra of SNe 2012A, 1999em, 2005cs and 2009bw. The error bars for the velocity of  $H\alpha$  in SN 2012A are smaller than the points.

If we take the velocity of the Sc II 6245 Å line with its low optical depth as representative of the photospheric expansion velocity, we find that SN 2012A has an intermediate velocity between SNe 1999em and 2005cs (cf. Figure 13).

#### 4.4 Extinction

The four high resolution spectra ( $R \sim 17000$ ) taken with the REOSC Echelle Spectrograph, mounted at Copernico

1.82m Telescope, were used to search for the presence of narrow interstellar and circumstellar lines.

We identified both the Galactic and the host galaxy Na I D absorption components. For the Galactic component, detected at  $-20 \text{ km s}^{-1}$ , we measured the EW of the D<sub>1</sub> and D<sub>2</sub> lines, finding  $\text{EW}(D_1)=0.127\pm 0.005 \text{ \AA}$  and  $\text{EW}(D_2)=0.204\pm 0.005 \text{ \AA}$ . The intensity of the Na I D lines is correlated with the amount of extinction. Applying the relation derived by Poznanski, Prochaska, & Bloom (2012) for both lines combined (their equation (9)), we obtain  $E(B - V) = 0.034_{-0.006}^{+0.008} \text{ mag}$ . This estimate is in excellent agreement with the value derived from the Schlafly & Finkbeiner (2011) recalibration of the Schlegel, Finkbeiner, & Davis (1998) infrared-based dust map that is  $E(B - V) = 0.028 \text{ mag}$ .

The weak absorption features measured at a velocity of  $\sim 770 \text{ km s}^{-1}$  correspond to the Na I D in the host galaxy. These features show multiple components, for a total  $\text{EW}(D_1+D_2) = 0.03\pm 0.01 \text{ \AA}$ . Based on this analysis we can adopt a total, Galactic plus host, extinction in the direction of SN 2012A of  $E(B - V) = 0.037_{-0.006}^{+0.008} \text{ mag}$ , or  $A_V = 0.12 \text{ mag}$  and  $A_B = 0.15 \text{ mag}$  for a standard  $R_V = 3.1$  reddening law (Cardelli, Clayton, & Mathis 1989).

In our first Echelle spectrum, the Galactic Ca II H&K absorptions (Ca II H 3968.5 Å and Ca II K 3933.7 Å) are also detected at  $-20 \text{ km s}^{-1}$ , along with two absorption features that we identify with Ca II H&K in the host galaxy (Figure 14). The Ca II H&K SN host absorption systems have multiple components (at least five) with a mean recessional velocity of  $765\pm 3 \text{ km s}^{-1}$  and  $771\pm 3 \text{ km s}^{-1}$  respectively. The association of this complex absorption systems to NGC 3239 (as well as the weak Na I D features at  $\sim 770 \text{ km s}^{-1}$ ) is consistent with the reported galaxy recessional velocity ( $753 \pm 3 \text{ km s}^{-1}$ ; de Vaucouleurs et al. 1991), and that measured from the H II region close to the SN position ( $807 \pm 1 \text{ km s}^{-1}$ ).

#### 4.5 Host environment properties

We exploited our high resolution spectra to derive the oxygen abundance of the H II region near SN 2012A using the relations described by Pettini & Pagel (2004). These authors calibrate the oxygen abundances of extragalactic H II regions for which the oxygen abundance was determined with the direct  $T_e$  method against the  $N2$  and  $O3N2$  indices:  $N2 \equiv \log ([\text{N II}]6583 \text{ \AA}/H\alpha)$  and  $O3N2 \equiv \log \{ ([\text{O III}]5007 \text{ \AA}/H\beta)/([\text{N II}]6583 \text{ \AA}/H\alpha) \}$ . These indices have the advantage over other types of calibrations of a small wavelength separation between the lines, and hence are less sensitive to extinction and to spectral flux calibration. Pettini & Pagel (2004) remark that the  $N2$  index yields estimates of the oxygen abundance accurate to within  $\sim 0.4$  dex at the 95% confidence level while with the  $O3N2$  index the oxygen abundance can be deduced to within  $\sim 0.25$  dex (again, at the 95% confidence level).

In order to obtain the spectrum of the SN host H II region, we have oriented the slit of the spectrograph at a position angle  $\text{PA} = -45^\circ$  and extracted the H II region spectrum adjacent to the SN trace. We flux calibrated this spectrum (see Figure 15) using spectrophotometric standards observed in the same night (MJD = 55936.95, at +4 d). Nebular line fluxes for [N II] 6583 Å,  $H\alpha$ , [O III] 5007 Å and  $H\beta$ ,

**Table 9.** Measured blackbody temperatures and expansion velocities in  $\text{km s}^{-1}$  (from the minima of P-Cygni absorptions) for SN 2012A. Estimated uncertainties are in parentheses.

Date	MJD	Phase [d]	$T_{bb}$ [K]	Fe II 5169 Å	Sc II 5527 Å	Sc II 6245 Å	Na ID <sup>1</sup>	H $\alpha$	Ba II 6142 Å
20120109	55936.14	3.1	12700 (200)				[8574 (200)]	10228 (200)	
20120115	55941.21	8.2	11430 (200)						
20120117	55943.14	10.1	10900 (200)						
20120118	55944.03	11.0	9650 (300)						
20120118	55944.14	11.1	9400 (300)				[6013 (200)]	8090 (200)	
20120118	55944.98	12.0	9680 (300)				[5896 (200)]	8108 (200)	
20120119	55945.19	12.2	9310 (300)				[5957 (200)]	7994 (100)	
20120120	55946.06	13.1	9216 (300)					7939 (100)	
20120121	55947.00	14.0	9090 (300)	5196 (120)				7569 (100)	
20120121	55947.98	15.0	9136 (300)	5432 (120)				7309 (100)	
20120123	55949.98	17.0	8280 (300)	4929 (100)				7286 (50)	
20120124	55950.97	18.0	7590 (300)	4900 (80)				6934 (50)	
20120126	55952.15	19.1	7270 (300)	4597 (100)				7021 (100)	
20120127	55953.03	20.0	7200 (300)	4536 (50)				6866 (80)	
20120129	55955.97	22.9	6500 (500)	4059 (50)				6651 (50)	
20120130	55956.92	23.9	6600 (500)	3913 (100)				6596 (50)	
20120205	55962.94	29.9	6650 (400)	3943 (200)				6532 (200)	
20120210	55968.11	35.1	6300 (400)	3247 (50)	3804 (100)	3575 (200)	3664 (150)	6185 (50)	2783 (200)
20120213	55970.94	37.9	6200 (400)	3189 (100)	3563 (150)	3421 (200)	3890 (150)	6295 (100)	2813 (200)
20120218	55975.94	42.9	6400 (500)	3340 (50)	3574 (100)	3182 (100)	3840 (100)	6094 (50)	2861 (200)
20120222	55980.00	47.0	6500 (500)	3224 (50)	3351 (80)	3192 (80)	3920 (100)	6048 (50)	2700 (200)
20120225	55982.99	50.0	6500 (500)	2841 (50)	3146 (80)	3229 (80)	3840 (100)	5934 (50)	2675 (200)
20120228	55985.92	52.9	6350 (400)	2690 (50)	2977 (80)	2894 (80)	3743 (100)	5710 (50)	2325 (200)
20120311	55998.09	65.1	6200 (400)	2702 (50)	2809 (80)	2600 (100)	3630 (100)	5532 (50)	2193 (200)
20120313	55999.17	66.2	6200 (300)	2668 (50)	2815 (100)	2482 (100)	3756 (100)	5511 (50)	2072 (100)
20120313	55999.18	66.2	5900 (500)					5560 (50)	2260 (200)
20120315	56000.09	67.1	6200 (500)						
20120315	56001.88	68.9	6100 (500)	2417 (50)	2627 (150)	2318 (200)	3432 (150)	5345 (80)	2066 (200)
20120317	56003.91	70.9	6200 (500)	2354 (50)	2489 (80)	2300 (100)	3500 (100)	5326 (50)	2119 (200)
20120325	56012.01	79.0	6000 (500)	2264 (100)	2380 (150)	2033 (200)	3253 (150)	5198 (80)	1802 (300)
20120327	56013.84	80.8	6000 (500)	2261 (50)	2315 (80)	2030 (100)	3300 (100)	5112 (50)	1807 (200)
20120329	56015.83	82.8	5800 (500)	2303 (80)	2348 (150)	1983 (200)	3272 (150)	5185 (80)	1832 (300)
20120331	56017.90	84.9	5900 (500)	2174 (50)	2391 (80)	2030 (100)	3330 (100)	5176 (50)	1885 (200)
20120412	56029.82	96.8		1971 (150)	2300 (250)	2000 (300)	3288 (200)	4976 (200)	
20120422	56040.06	107.1		1930 (150)	2239 (200)	1900 (400)	3453 (300)	4897 (100)	1890 (30)
20120424	56041.91	108.9		1930 (100)	1961 (100)	1953 (300)	3400 (200)	4582 (150)	1890 (30)
20120427	56044.94	111.9		2433 (100)	2300 (250)	1800 (300)	3650 (300)	4591 (150)	
20120501	56048.89	115.9		1943 (120)	2300 (250)		3533 (300)	4701 (150)	
20120515	56062.87	129.9			2400 (200)	1500 (200)	3460 (300)	4641 (150)	
20120515	56062.89	129.9		1901 (150)	1950 (100)	2000 (400)	3212 (300)	4280 (150)	

<sup>1</sup>Note: the velocity in square brackets are those of the line identified as He I 5876 Å.

were measured (Table 10) and we derived  $N2 = -1.43 \pm 0.03$  and  $O3N2 = 2.17 \pm 0.04$ . From these indices we estimated the SN 2012A host oxygen abundance to be  $12 + \log(O/H) = 8.11 \pm 0.09$  (using  $N2$ ) and  $12 + \log(O/H) = 8.04 \pm 0.01$  (using  $O3N2$ ).

Several authors have recently used the Pettini & Pagel (2004) indices to obtain estimates of the environment metallicities for SNe II (Prantzos & Boissier 2003; Prieto, Stanek, & Beacom 2008; Anderson et al. 2010; Sanders et al. 2012; Stoll et al. 2012), finding some evidence that the hosts of type Ib/c SNe have higher metallicity than those of type II and type Ia SNe. The environment of type II SNe show a mean oxygen abundances  $12 + \log(O/H) = 8.58$  (with a dispersion of  $\sim 0.75$  dex), as derived by Anderson et al. (2010) for a sample of about fifty type

**Table 10.** Flux measurements of nebular lines in the Echelle spectrum of H II region near SN 2012A at +4 d.

Line	Flux [ $\times 10^{-14} \text{ erg cm}^{-2} \text{ s}^{-1}$ ]
[N II] 6583 Å	0.41
H $\alpha$	11.00
[O III] 5007 Å	19.60
H $\beta$	3.55

II SNe, or 8.65 measured for a sample of 36 type II SNe observed in the first year of the Palomar Transient Factory

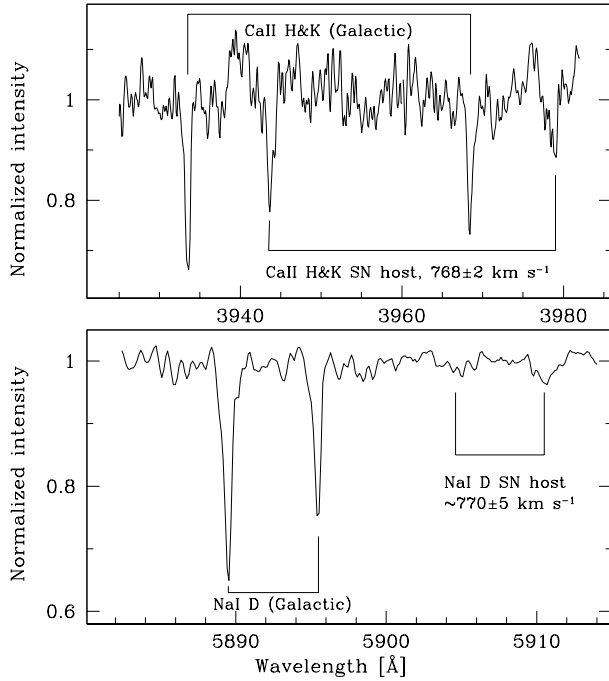


**Figure 14.** Echelle spectrum of SN 2012A at MJD = 55936.95 (+4 d) in the Ca II H&K (top panel) and Na I D (bottom panel) wavelength regions. Galactic Ca II H&K and Na I D absorption features are marked. The Ca II H&K SN host absorption systems have multiple components with a mean recessional velocity of  $768 \pm 2 \text{ km s}^{-1}$ . Weak absorption features measured at a mean velocity of  $\sim 770 \text{ km s}^{-1}$  and corresponding to the Na I doublet of the host galaxy are also detected.

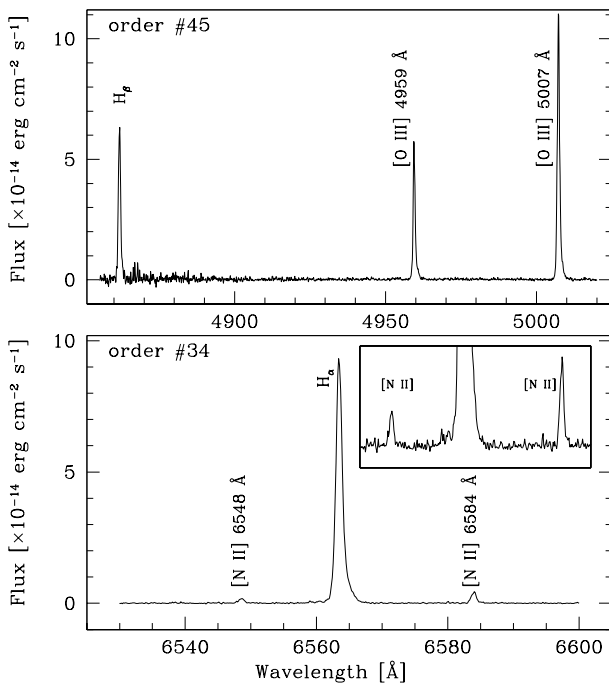


**Figure 15.** Sections of Echelle spectrum of H II region near SN 2012A at MJD = 55936.95 (+4 d), order #45 (top panel), showing nebular lines  $H\beta$  and [O III] 4959, 5007 Å, and order #34 (bottom panel), with nebular lines  $H\alpha$  and [N II] 6548, 6583 Å. The insert shows a zoomed view of [N II] 6548, 6583 Å lines.

SN search (Law et al. 2009; Arcavi et al. 2010; Stoll et al. 2012).

Our measurement of the environment metallicity places SN 2012A in the metal-poor tail of the distribution of oxygen abundances for the type II SNe (cf. Figure 9 in Stoll et al. 2012), which includes samples by Prieto, Stanek, & Beacom (2008); Anderson et al. (2010); Stoll et al. (2012). We may notice that Prieto, Stanek, & Beacom (2008) discuss the properties of some SNe which exploded in metal-poor environments, including SN 2006jc (a peculiar SN Ib/c with strong He I emission lines), SN 2007I (a broad-lined SN Ic) and SN 2007bk (a 91T-like SN Ia). A number of type II SNe have also been discovered in metal-poor galaxies (see the list in Prieto, Stanek, & Beacom 2008). However, to our knowledge, a follow-up monitoring campaign for these SNe was not conducted.

## 5 PROGENITOR

### 5.1 Direct progenitor detection

Since the advent of the *Hubble Space Telescope* (*HST*) and 8-m class ground-based telescopes with publicly searchable archives, the direct detection of CC SN progenitors has become possible for nearby ( $\lesssim 30 \text{ Mpc}$ ) SNe (as reviewed in Smartt 2009a). With this in mind, we searched for pre-explosion images of NGC 3239 in which we might detect and constrain the progenitor of SN 2012A. While there are no *HST* images of NGC 3239, the galaxy was observed prior to the explosion of SN 2012A with the Near InfraRed Imager and Spectrometer (NIRI) on the Gemini North Telescope<sup>4</sup>.

NGC 3239 was observed on 2006 May 13 in  $K'$  with the f/14 camera on NIRI, which has a pixel scale of  $0.05 \text{ arcsec pix}^{-1}$  across a  $51 \times 51 \text{ arcsec}^2$  field of view. The adaptive optics (AO) facility ALTAIR was used when taking these observations, giving a corrected FWHM for point sources of around  $0.15''$ , compared to the natural seeing of between 0.4 and 0.5 arcsec. Multiple short exposures were used to avoid saturating the detector on the near-infrared sky. As the target was a crowded field with extended background structure, a separate off-source field was observed in between observations of the target to allow the sky background to be subtracted. A total on-source exposure time of 600s was used, with the individual frames being reduced and co-added within the IRAF GEMINI package. A second set of images of NGC 3239 were obtained with the same instrument and filter on the same night, but using the f/6 camera to cover a larger field of view at the expense of a coarser pixel scale ( $120 \times 120 \text{ arcsec}^2$  with  $0.12 \text{ arcsec pix}^{-1}$ ). ALTAIR was not used for these data, which had a FWHM of  $\sim 0.5 \text{ arcsec}$ . As before, the images were reduced and co-added using the GEMINI package, to give an on-source exposure time of 270s.

Ideally, to identify a progenitor in the pre-explosion  $K'$ -band image we would use either an AO image of the SN, or an image from *HST*. Unfortunately, we did not obtain an AO image of SN 2012A with our progenitor program, and instead we used the best natural seeing image from our follow-up campaign to astrometrically align to the pre-explosion data. The  $J$ -band image obtained with NOT+NOTCAM

<sup>4</sup> Programme ID: GN-2006A-DD-2, PI: Michaud

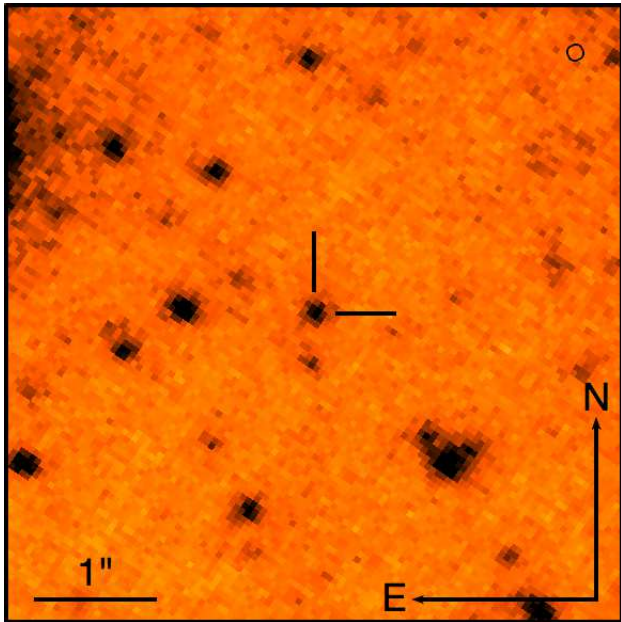


**Figure 16.** A section of the pre-explosion Gemini N + NIRI + f/14  $K'$ -filter image of NGC 3239, centered on the progenitor candidate. The transformed SN coordinates are at the intersection of the tick marks. Scale and orientation are as indicated in the figure; the circle in the upper right corner of the image has a radius corresponding to the 63 mas uncertainty in the SN position.

on 2012 May 6 is reasonably deep and has a FWHM of 0.5 arcsec, and is therefore suitable for our purpose.

We first aligned the NOTCAM  $J$ -band image directly to our pre-explosion  $K'$  f/14 image. 27 sources common to both images were identified, and their positions measured. IRAF GEOMAP was then used to derive a transformation between the two images, allowing for shifts, rotation and a change in pixel scale (i.e. the rscale fit geometry in GEOMAP). After rejecting two obvious outliers from the fit, the rms error on the transformation was 63 mas. We measured the SN position in the post explosion image using the average of the three different centering algorithms (centroid, gauss and filter) within IRAF PHOT, taking their standard deviation (9 mas) as the error.

Using the pixel coordinates of the SN in the NOTCAM  $J$ -band image together with our geometric transformation, we determined the pixel coordinates of the SN in the pre-explosion f/14 image. A source is visible at this position, as can be seen in Figure 16. As before, we measured the position of the source with three different algorithms, taking their standard deviation (1 mas) as the error. The offset between the measured pixel coordinates of the progenitor candidate and the transformed SN pixel coordinates is only 16 mas, well within our combined astrometric uncertainty of 64 mas. We hence find the progenitor candidate to be formally coincident with SN 2012A.

To determine the photometric zero point of the f/14 image, we first photometrically calibrated the f/6 image to the 2MASS system using aperture photometry of two isolated point sources in the field, for which magnitudes were listed in the 2MASS catalog. We then performed aperture photometry on five sources common to both the f/6 and f/14 images, and used these to set the zeropoint of the latter in

the 2MASS system. Adding the error from both steps in quadrature, we find an uncertainty of 0.09 mag in the zeropoint of the f/14 image. We performed aperture photometry on the progenitor candidate, and using the determined zeropoint found a magnitude of  $K' = 20.29 \pm 0.13$  mag.

For our adopted distance to NGC 3239 ( $29.96 \pm 0.15$  mag) the progenitor has an absolute magnitude of  $K' = -9.67 \pm 0.20$  mag. The foreground extinction ( $A_V = 0.115$  mag, see Section 4.4) implies an extinction of only 0.01 mag in  $K'$ , with a negligible effect on the progenitor analysis. To determine a progenitor luminosity, we need to know the bolometric correction to the progenitor  $K'$  magnitude. As bolometric corrections vary as a function of temperature (or spectral type), we must assume a temperature range for the progenitor. The fact that SN 2012A is a type IIP SN, with a plateau phase powered by recombination of hydrogen, implies that its progenitor must have been a hydrogen-rich red supergiant. Hence we have taken a range of bolometric corrections to the  $V$ -band and  $V - K'$  colours based on synthetic photometry of MARCS model spectra (Gustafsson et al. 2008), appropriate for RSGs with temperatures between 3400 K and 4250 K (Fraser et al. in prep). Over this temperature range, we find that  $(V - K') + BC_V$  varies between +2.89 mag for the hottest model to +2.29 mag for the coolest.

Applying the average of these values to our progenitor  $K'$  magnitude, we find a bolometric magnitude of  $-7.08 \pm 0.36$  mag, where the error is a combination of the photometric error, the uncertainty in the distance, and the range of plausible bolometric corrections. This corresponds to a luminosity of  $\log L/L_\odot = 4.73 \pm 0.14$  dex.

To convert the derived luminosity for the progenitor candidate to a mass, we must compare it with the predictions of stellar evolutionary models. We have made this comparison to models from the STARS code (Eldridge et al. 2008 and references therein), which are computed with standard prescriptions for burning, mass loss, overshooting etc. Solar metallicity models were used, although as shown by Smartt et al. (2009b) the precise metallicity has negligible effect on the final luminosity of the models. Smartt et al. also compare the output of the STARS code with other stellar evolutionary codes, and find good agreement.

Comparing the luminosity of the progenitor to the luminosity of stellar evolutionary models at the beginning of core neon burning, we find that a  $10.5 M_\odot$  progenitor is the best match. The lower limit to the luminosity is 4.6 dex, corresponding to a progenitor with a zero-age main sequence mass of  $8.5 M_\odot$ . If the progenitor were less massive than this, it would also likely be much more luminous, having undergone second dredge-up, as discussed by Fraser et al. (2011). We set a conservative upper limit to the progenitor mass of  $15 M_\odot$  from comparing the maximum luminosity of the progenitor to the luminosity of the STARS models at the end of core He burning.

The progenitor mass found for SN 2012A,  $10.5^{+4.5}_{-2} M_\odot$ , is comparable to the low progenitor masses found for other type IIP SNe (Smartt 2009a). We note that the fact that our progenitor detection is in  $K$  makes it much less sensitive to extinction. As found for SN 2012aw by Fraser et al. (2012) and Van Dyk et al. (2012), and discussed in detail by Kochanek, Khan & Dai (2012), there is evidence that some type IIP SNe have circumstellar dust which is destroyed in

the SN explosion, and so the extinction towards the SN cannot be taken as a measure of the extinction towards the progenitor. However, given that the typical extinction of a few magnitudes in  $V$  seen towards Galactic RSGs by Levesque et al. (2005) would correspond to a few *tenths* of a magnitude in  $K$  (a value which is well within our uncertainties), this is not of great concern for this SN.

## 5.2 Hydrodynamical modeling

An independent approach to constrain the SN 2012A progenitor's physical properties at the explosion, namely the ejected mass, the progenitor radius and the explosion energy, is through the hydrodynamical modeling of the SN observables, i.e. bolometric light curve, evolution of line velocities and continuum temperature at the photosphere. We adopt the same approach used for other CC SNe (e.g. SNe 2007od, 2009bw, and 2009E; see Inserra et al. 2011, 2012, and Pastorello et al. 2012), in which a simultaneous  $\chi^2$  fit of the observables against model calculations is used.

For computing the models we employ two codes: i) a semi-analytic code (described in detail by Zampieri et al. 2003) which solves the energy balance equation for an envelope with constant density in homologous expansion, and ii) the general-relativistic, radiation-hydrodynamics Lagrangian code presented in Pumo, Zampieri, & Turatto (2010) and Pumo & Zampieri (2011). The latter is able to simulate the evolution of the physical properties of the ejected material and the behavior of the main observables up to the nebular phase, solving the equations of relativistic radiation hydrodynamics for a self-gravitating fluid which interacts with radiation, taking into account both the gravitational effects of the compact remnant and the heating effects linked to the decays of the radioactive isotopes synthesized during the CC SN explosion.

The semi-analytic code is used to perform a preparatory study aimed at individuating the parameter space describing the CC SN progenitor at the explosion and, consequently, to guide the more realistic, but time consuming simulations performed with the general-relativistic, radiation-hydrodynamics code.

In performing the  $\chi^2$  fit, we do not include the observational data taken at phase  $< 20$  days that is approximately the time needed for the bolometric light curve to relax to the plateau. At earlier epochs all the observables are significantly affected by emission from the outermost shell of the ejecta (cf. Pumo & Zampieri 2011). After shock passage, this shell, that contains only a small fraction of the envelope mass, is accelerated to very high velocities and is not in homologous expansion. The structure, evolution and emission properties of this shell cannot be probed in our simulations because at present we adopt an *ad hoc* initial density profile, not consistently derived from a post-explosion calculation.

In addition, we point out that our modeling is appropriate when the emission from the CC SN is dominated by the expanding ejecta with no contribution from interaction with a dense circumstellar medium (CSM). In fact, as shown by Moriya et al. (2011), the presence of a CSM around the SN (i.e. the remnant of the red supergiant wind) can heavily affect the early evolution of the light curves. In particular, following the collision of the SN ejecta with the CSM, kinetic energy is converted to thermal energy, which is emitted as

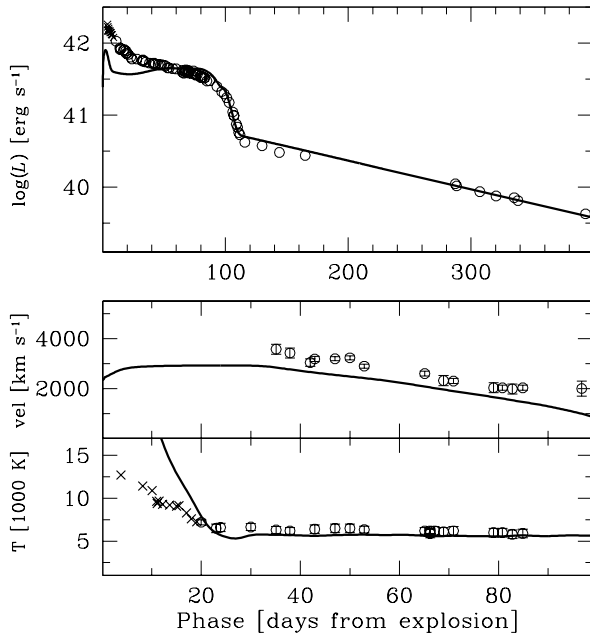


**Figure 17.** Comparison of the evolution of the main observables of SN 2012A with the best-fitting model computed with a general-relativistic, radiation-hydrodynamics code (total energy 0.48 foe, initial radius  $1.8 \times 10^{13}$  cm, envelope mass  $12.5 M_{\odot}$ ). Top, middle, and bottom panels show the bolometric light curve, the photospheric velocity, and the photospheric temperature as a function of time. To better estimate the photosphere velocity from observations, we use the minima of the profile of the Sc II lines. The crosses indicate the observational data taken at early phases ( $< 20$  d) not considered in the  $\chi^2$  fit (see text for details).

radiation. As a consequence, the SN appears *UV* bright at early times as was observed in SN 2009kf (Botticella et al. 2010). A similar effect may explain the bright initial *UV* peak of SN 2012A.

The interaction of the SN ejecta with a CSM can also have signatures either in the radio or in the  $X$ -ray wavelength regions (cf. for example Chakraborti et al. 2013). As already remarked in Section 3.4, SN 2012A was not detected in the radio domain (Stockdale et al. 2012), while the  $X$ -ray detection corresponds to a negligible contribution to the bolometric flux (?). Hence we can safely state that in SN 2012A the contribution from ejecta-CSM interaction to the observed luminosity is negligible.

Based on the adopted explosion epoch (Section 3.1), bolometric luminosity and nickel mass ( $M(^{56}\text{Ni}) = 0.011 M_{\odot}$ , Section 5), the best-fitting model shown in Figure 17 has a total (kinetic plus thermal) energy of 0.48 foe (1 foe  $\equiv 10^{51}$  erg), initial radius of  $1.8 \times 10^{13}$  cm, and envelope mass of  $12.5 M_{\odot}$ . This corresponds to a total stellar mass at the time of explosion of  $\sim 14 M_{\odot}$ , if we account for a  $1.5 M_{\odot}$  compact remnant. The estimated uncertainty on the total stellar mass is about 15%.

From Figure 17 (middle panel) one can notice a small ( $\sim 10\%$ ) systematic offset between the observed photospheric velocity and the modeling. This discrepancy could be reduced, at least for the first two months of evolution, by adopting for the model a slightly higher total energy of 0.5 – 0.6 foe and an envelope mass between 10 and  $13 M_{\odot}$ .

However in this case we would get a worse fit to the observed light curve, with a slightly shorter (by about 3 d) plateau.

## 6 DISCUSSION

SN 2012A is an excellent SN for intensive study thanks to a number of reasons.

Our detailed photometric and spectroscopic optical monitoring, combined with near-infrared photometry and the early *UV* photometry from *Swift*, allow us to reconstruct the evolution of the bolometric luminosity and derive accurate estimates of the expansion velocity and photospheric temperature. From our photometric converge during the radioactive tail of the light curve we could measure a  $^{56}\text{Ni}$  mass. Our effort was facilitated by a number of favorable circumstances. Thanks to the high resolution spectra we can derive an accurate estimate of the line of sight extinction, which turned out to be very low. Also, the pre-discovery non-detections and early discovery (in the rising branch of the light curve) allow to constrain the epoch of the explosion, making SN 2012A an ideal case to test hydrodynamic models. Most importantly, thanks to fortuitous deep, high resolution, archival images and the relatively nearby distance to the host galaxy, we could directly identify a progenitor candidate for SN 2012A.

Here we focus on the attempts to constrain the progenitor mass using the two different approaches, namely the direct detection of the progenitor in pre-explosion archival images and the hydrodynamical modeling of the expanding ejecta.

It has been noted that, at least in some cases, the two methods lead to very different results, with the hydrodynamic modeling-derived mass being systematically higher than that obtained from direct measurements (Smartt 2009a). For instance, through modeling of SN 2005cs and SN 2004et, Utrobin & Chugai (2008, 2009) found progenitor masses of  $\sim 20$  and  $\sim 30 M_{\odot}$  respectively. These masses are a factor of 2–3 time larger than the values obtained from an analysis of pre-explosion imaging,  $\sim 7$  and  $\sim 9 M_{\odot}$  respectively (Smartt et al. 2009b). In other cases the discrepancy is not so large (cf. Table 7 in Maguire et al. 2010b), but always noticeable.

This is also the case for SN 2012A where although the two values are fully consistent within the errors, the best estimate from the hydrodynamic modeling ( $\sim 14 \pm 2 M_{\odot}$  including the compact remnant) is about 30% higher than the direct mass estimate ( $10.5_{-2}^{+4.5} M_{\odot}$ ).

Utrobin & Chugai (2009) speculated that hydrodynamic models could overestimate the progenitor mass due to the neglect of multi-dimensional effects. They argued that explosion asymmetries, which are not included in the modeling, may explain the disagreement between progenitor mass determinations for SN 2004et. In that case, a possible bipolar structure was suggested based on the line profile of the  $\text{H}\alpha$  and  $[\text{O I}]$  6300, 6364 Å nebular emissions (Chugai 2006). A similar feature, namely a double peaked  $\text{H}\alpha$  profile observed in late-stage spectra of SN 2012A (see Section 4.1) could also be an evidence of the asymmetry in the SN ejecta or, most likely, in the radioactive  $^{56}\text{Ni}$  bubble.

For direct progenitor detections, a major source of uncertainty is the presence (or absence) of circumstellar

dust. In the case of SN 2012aw, Fraser et al. (2012) and Van Dyk et al. (2012) estimated a very low extinction after explosion, but found evidence for pre-existing circumstellar dust which was destroyed in the explosion. For SN 2012A, the possible effect of dust is reduced because the progenitor luminosity was derived from a near-infrared magnitude. A separate source of error arises from the stellar evolutionary models used. As emphasized by Smartt et al. (2009b), a different treatment of mixing processes can change the stellar core mass and hence affect the final luminosity. In particular, the choice of convective overshooting parameter will alter the final configuration of stellar models, with lower overshooting leading to lower luminosity progenitors for a given mass.

As an independent constraint of the progenitor mass, we measured the relative intensities of emission lines in the nebular spectrum and compared these values with the predictions of the spectral synthesis model of Jerkstrand et al. (2012). We found that the  $[\text{OI}]$  and  $\text{Na I D}$  line intensities (relative to the total radioactive energy input) are close to the predicted values for a  $15 M_{\odot}$  star, also consistent with the estimates given above.

In conclusion, all evidence points toward a moderate  $\sim 10 - 15 M_{\odot}$  red supergiant star as the progenitor of SN 2012A.

## 7 SUMMARY

We have presented our extensive data set for SN 2012A, starting from a few days after shock breakout, and covering over one year of evolution to when the SN had completely entered the nebular phase. The collected observations, which consist of *UBVRIJHKugriz* photometry, low and high-resolution optical spectroscopy and a near-*IR* spectrum, make this type IIP SN one of the most comprehensively observed ever.

The analysis of the observations of SN 2012A show that this is a type IIP supernova with own identity. In particular the plateau appears shorter than in prototypical type IIP SNe, while the plateau luminosity is never really constant. The luminosity in the radioactive tail is moderate, which implies a  $^{56}\text{Ni}$  mass which is intermediate between those of prototypical type IIP and faint IIP SNe. In the future, a larger sample of such well studied events exploring the subtle diversity among “normal” SNe IIP, may help to elucidate the details of the explosion mechanism and progenitor properties.

Comparing the bolometric light curve of SN 2012A with that of SN 1987A, we derive for SN 2012A an ejected  $^{56}\text{Ni}$  mass of  $0.011 \pm 0.004 M_{\odot}$ . This value is intermediate between SN 1999em and the  $^{56}\text{Ni}$ -poor SN 2005cs (Pastorello et al. 2009), and close to that of SN 2009bw (Inserra et al. 2012).

The high-resolution spectra allow us to estimate the metallicity of a H II region close to the site of SN 2012A. The estimated oxygen abundance is  $12 + \log(\text{O}/\text{H}) = 8.04 \pm 0.01$  (using *O3N2*). The derived metallicity shows that the host of SN 2012A, was in the metal-poor tail of the distribution for the hosts of type II SNe.

A double peaked structure in  $\text{H}\alpha$  profile clearly arises in SN 2012A by day +112 and disappears at around day +173. This may indicate a bipolar structure of the hydrogen

excitation and can be interpreted as a result of the asymmetric ejection of  $^{56}\text{Ni}$  in the spherically-symmetric envelope (Chugai 2006).

The direct detection of the progenitor of SN 2012A in archival images indicates that the progenitor star had a moderate mass of  $10.5_{-2}^{+4.5} M_{\odot}$ . The hydrodynamical modeling of the explosion (bolometric luminosity,  $T_{bb}$  and expansion velocity evolution) and the analysis of [O I] and Na I D nebular lines fluxes (Jerkstrand et al. 2012) seem to favor a slightly higher mass, around 14–15  $M_{\odot}$ . Considering the errors on the observables, the assumptions of the evolutionary models, the approximations in the hydrodynamical model, and the uncertainties introduced by a different  $^{56}\text{Ni}$  mass for SN 2012A compared to that in the spectral models of Jerkstrand et al. (2012), we find that all three mass estimates are consistent with each other.

## ACKNOWLEDGMENTS

L.T., E.C., A.P., S.B., F.B. and M.T. are partially supported by the PRIN-INAF 2011 with the project “Transient Universe: from ESO Large to PESSTO”. We acknowledge the TriGrid VL project and the INAF-Astronomical Observatory of Padua for the use of computer facilities. M.L.P. acknowledges the financial support from the PRIN-INAF 2009 “Supernovae Variety and Nucleosynthesis Yields” (P.I. S. Benetti). V.S. acknowledges financial support from Fundação para a Ciência e a Tecnologia (FCT) under program Ciência 2008 and the research grant PTDC/CTE-AST/112582/2009. S.T. acknowledges support by the TRR 33 “The Dark Universe” of the German Research Foundation. G.P. and F.B. acknowledge support from “Millennium Center for Supernova Science” (P10-064-F), with input from “Fondo de Innovación para la Competitividad del Ministerio de Economía, Fomento y Turismo de Chile”. G.P. acknowledges partial support by “Proyecto interno UNAB DI-303-13/R”.

This paper is based on observations collected at the Copernico 1.82m Telescope and Schmidt 67/92 Telescope operated by INAF - Osservatorio Astronomico di Padova at Asiago, Italy, Galileo 1.22m Telescope operated by Department of Physics and Astronomy of the University of Padova at Asiago, Italy. Data was provided by the 2.56m Nordic Optical Telescope operated by The Nordic Optical Telescope Scientific Association (NOTSA), by 2.5 Isaac Newton Telescope and 4.3m William Herschel Telescope operated by the Isaac Newton Group of Telescopes, by the 3.6m Italian Telescopio Nazionale Galileo operated by the Fundación Galileo Galilei - INAF on the island of La Palma. The paper made also use of observations collected at the Observatoire de Haute-Provence 1.93m Telescope operated by Université d’Aix-Marseille and CNRS, France, at the Calar Alto Observatory 2.2m Telescope operated jointly by the Max-Planck-Institut für Astronomie (MPIA) in Heidelberg, Germany, and the Instituto de Astrofísica de Andalucía (CSIC) in Granada/Spain, at NTT, Trappist and REM Telescopes operated by European Southern Observatory (ESO) and Prompt Telescopes operated by Cerro Tololo Inter-American Observatory (CTIO) in Chile.

## REFERENCES

- Anderson J. P., Covarrubias R. A., James P. A., Hamuy M., Habergham S. M., 2010, *MNRAS*, 407, 2660  
 Arcavi I., et al., 2010, *ApJ*, 721, 777  
 Asplund M., Grevesse N., Sauval A. J., Scott P., 2009, *ARA&A*, 47, 481  
 Barbon R., Benetti S., Cappellaro E., Patat F., Turatto M., Iijima T., 1995, *A&AS*, 110, 513  
 Baron E., Nugent P. E., Branch D., Hauschildt P. H., 2004, *ApJ*, 616, L91  
 Benetti S., et al., 2001, *MNRAS*, 322, 361  
 Bersten M. C., et al., 2012, *ApJ*, 757, 31  
 Blinnikov S., Lundqvist P., Bartunov O., Nomoto K., Iwamoto K., 2000, *ApJ*, 532, 1132  
 Botticella M. T., et al., 2010, *ApJ*, 717, L52  
 Cardelli J. A., Clayton G. C., Mathis J. S., 1989, *ApJ*, 345, 245  
 Chakraborti S., et al., 2013, arXiv, arXiv:1302.7067  
 Chonis T. S., Gaskell C. M., 2008, *AJ*, 135, 264  
 Chugai N. N., 1991, *SvA*, 35, 171  
 Chugai N. N., Fabrika S. N., Sholukhova O. N., Goranskij V. P., Abolmasov P. K., Vlasyuk V. V., 2005, *AstL*, 31, 792  
 Chugai N. N., 2006, *AstL*, 32, 739  
 D’Andrea C. B., et al., 2010, *ApJ*, 708, 661  
 Danziger I. J., 1988, *snoy.conf*, 3  
 Dessart L., Hillier D. J., 2005, *A&A*, 439, 671  
 de Vaucouleurs G., de Vaucouleurs A., Corwin H. G., Jr., Buta R. J., Paturel G., Fouque P., 1991, *S&T*, 82, 621  
 Eldridge J.J., Izzard R.G., Tout C.A., 2008, *MNRAS*, 384, 1109  
 Elmhamdi A., et al., 2003, *MNRAS*, 338, 939  
 Elmhamdi A., Chugai N. N., Danziger I. J., 2003, *A&A*, 404, 1077  
 Falk S. W., Arnett W. D., 1977, *ApJS*, 33, 515  
 Fassia A., et al., 2001, *MNRAS*, 325, 907  
 Fitzpatrick E. L., 1999, *PASP*, 111, 63  
 Fraser M., Ergon M., Eldridge J.J. et al., 2011, *MNRAS*, 417, 1417  
 Fraser M., Maund J.R., Smartt S.J. et al., 2012, *ApJ*, 759, 13  
 Gerardy C. L., et al., 2001, *AAS*, 33, 1428  
 Grassberg E. K., Imshennik V. S., Nadyozhin D. K., 1971, *Ap&SS*, 10, 28  
 Gustafsson B., Edvardsson B., Eriksson K., Jørgensen U.G., Nordlund Å., Plez B. 2008, *A&A* 486, 951  
 Hamuy M., et al., 2001, *ApJ*, 558, 615  
 Hamuy M., Pinto P. A., 2002, *ApJ*, 566, L63  
 Harutyunyan A. H., et al., 2008, *A&A*, 488, 383  
 Kochanek C.S., Khan R., Dai X., 2012, *ApJ*, 759, 20  
 Hendry M. A., et al., 2005, *MNRAS*, 359, 906  
 Hendry M. A., et al., 2006, *MNRAS*, 369, 1303  
 Inserra C., et al., 2011, *MNRAS*, 417, 261  
 Inserra C., et al., 2012, *MNRAS*, 422, 1122  
 Jerkstrand A., Fransson C., Maguire K., Smartt S., Ergon M., Spyromilio J., 2012, *A&A*, 546, A28  
 Jones M. I., et al., 2009, *ApJ*, 696, 1176  
 Landolt A. U., 1992, *AJ*, 104, 340  
 Leonard D. C., et al., 2002, *AJ*, 124, 2490  
 Leonard D. C., et al., 2002, *PASP*, 114, 35  
 Levesque E. M., Massey P., Olsen K. A. G., Plez B., Jos-

- selin E., Maeder A., Meynet G., 2005, *ApJ*, 628, 973
- Li W., et al., 2011, *MNRAS*, 412, 1441
- Litvinova I. I., Nadezhdin D. K., 1983, *Ap&SS*, 89, 89
- Law N. M., et al., 2009, *PASP*, 121, 1395
- Maguire K., Kotak R., Smartt S. J., Pastorello A., Hamuy M., Bufano F., 2010, *MNRAS*, 403, L11
- Maguire K., et al., 2010, *MNRAS*, 404, 981
- Maguire K., et al., 2012, *MNRAS*, 420, 3451
- Moore, B., Newton, J., & Puckett, T. 2012, *Central Bureau Electronic Telegrams*, 2974, 1
- Moriya T., Tominaga N., Blinnikov S. I., Baklanov P. V., Sorokina E. I., 2011, *MNRAS*, 415, 199
- Mould J. R., et al., 2000, *ApJ*, 529, 786
- Nugent P., et al., 2006, *ApJ*, 645, 841
- Olivares E. F., et al., 2010, *ApJ*, 715, 833
- Osterbrock D. E., Waters R. T., Barlow T. A., Slangier T. G., Cosby P. C., 2000, *PASP*, 112, 733
- Otsuka M., et al., 2012, *ApJ*, 744, 26
- Pastorello A., et al., 2004, *MNRAS*, 347, 74
- Pastorello A., et al., 2006, *MNRAS*, 370, 1752
- Pastorello A., et al., 2009, *MNRAS*, 394, 2266
- Pastorello A., et al., 2012, *A&A*, 537, A141
- Pettini M., Pagel B. E. J., 2004, *MNRAS*, 348, L59
- Phillips M. M., Williams R. E., 1991, *supe.conf*, 36
- Pooley, D., & Immler, S. 2012, *The Astronomer's Telegram*, 3956, 1
- Poznanski D., et al., 2009, *ApJ*, 694, 1067
- Poznanski D., Prochaska J. X., Bloom J. S., 2012, *MNRAS*, 426, 1465
- Pozzo M., et al., 2006, *MNRAS*, 368, 1169
- Prantzos N., Boissier S., 2003, *A&A*, 406, 259
- Prieto J. L., Stanek K. Z., Beacom J. F., 2008, *ApJ*, 673, 999
- Prieto, J. L., Osip, D., & Palunas, P. 2012, *The Astronomer's Telegram*, 3863, 1
- Pritchard, T. A., Roming, P. W. A., Brown, P. J., Bayless, A. J., & Frey, L. H. 2013, *arXiv:1303.1190*
- Pumo M. L., Zampieri L., Turatto M., 2010, *MSAIS*, 14, 123
- Pumo M. L., Zampieri L., 2011, *ApJ*, 741, 41
- Quimby R. M., Wheeler J. C., Höflich P., Akerlof C. W., Brown P. J., Rykoff E. S., 2007, *ApJ*, 666, 1093
- Sanders N. E., et al., 2012, *ApJ*, 758, 132
- Schmidt B. P., Kirshner R. P., Eastman R. G., 1992, *ApJ*, 395, 366
- Schlafly E. F., Finkbeiner D. P., 2011, *ApJ*, 737, 103
- Schlegel D. J., Finkbeiner D. P., Davis M., 1998, *ApJ*, 500, 525
- Stockdale, C. J., Ryder, S. D., Van Dyk, S. D., et al. 2012, *The Astronomer's Telegram*, 3861, 1
- Smartt S. J., 2009, *ARA&A*, 47, 63
- Smartt S. J., Eldridge J. J., Crockett R. M., Maund J. R., 2009, *MNRAS*, 395, 1409
- Stanishev, V., & Pursimo, T. 2012, *Central Bureau Electronic Telegrams*, 2974, 3
- Stoll R., Prieto J. L., Stanek K. Z., Pogge R. W., 2012, *arXiv*, *arXiv:1205.2338*
- Tully R. B., 1988, *ngc..book*,
- Tully R. B., Rizzi L., Shaya E. J., Courtois H. M., Makarov D. I., Jacobs B. A., 2009, *AJ*, 138, 323
- Turatto M., Cappellaro E., Benetti S., Danziger I. J., 1993, *MNRAS*, 265, 471
- Turatto M., et al., 1998, *ApJ*, 498, L129
- Utrobin V. P., 2007, *A&A*, 461, 233
- Utrobin V. P., Chugai N. N., Pastorello A., 2007, *A&A*, 475, 973
- Utrobin V. P., Chugai N. N., 2008, *A&A*, 491, 507
- Utrobin V. P., Chugai N. N., 2009, *A&A*, 506, 829
- Van Dyk S.D., Cenko S.B., Poznanski D. et al., 2012, *ApJ*, 756, 131
- Walmswell J. J., Eldridge J. J., 2012, *MNRAS*, 419, 2054
- Woosley S. E., Hartmann D., Pinto P. A., 1989, *ApJ*, 346, 395
- Zampieri L., Pastorello A., Turatto M., Cappellaro E., Benetti S., Altavilla G., Mazzali P., Hamuy M., 2003, *MNRAS*, 338, 711
- Zampieri L., 2007, *AIPC*, 924, 358